20. Park, S., and Burghardt, T. P. (2002) Tyrosine mediated tryptophan ATP sensitivity in skeletal myosin. *Biochemistry 41*, 1436−1444.
21. Onishi, H., Konishi, K., Fujiwara, K., Hayakawa, K., Tanokura, M., Martinez, H. M., and Morales, M. F. (2000) On the tryptophan residue of smooth muscle myosin that responds to binding of nucleotide. *Proc. Natl. Acad. Sci. U.S.A. 97*, 11203−11208.
22. Malnasi-Csizmadia, A., Woolley, R. J., and Bagshaw, C. R. (2000) Resolution of conformational states of *Dictyostelium* myosin II motor domain using tryptophan (W501) mutants: implications for the open-closed transition identified by crystallography. *Biochemistry 39*, 16135−16146.
23. Gulick, A. M., Bauer, C. B., Thoden, J. B., and Rayment, I. (1997) X-ray structures of the MgADP, MgATPγS, and MgAMPPNP complexes of the *Dictyostelium discoideum* myosin motor domain. *Biochemistry 36*, 11619−11628.
24. Sasaki, N., Shimada, T., and Sutoh, K. (1998) Mutational analysis of the switch II loop of *Dictyostelium* myosin II. *J. Biol. Chem. 273*, 20334−20340.
25. Suzuki, Y., Yasunaga, T., Ohkura, R., Wakabayashi, T., and Sutoh, K. (1998) Swing of the lever arm of a myosin motor at the isomerization and phosphate-release steps. *Nature 396*, 380−383.
26. Lymn, R. W., and Taylor, E. W. (1971) Mechanism of adenosine triphosphate hydrolysis by actomyosin. *Biochemistry 10*, 4617−4624.
27. Levy, H. M., and Koshland, D. E. (1959) Mechanism of hydrolysis of adenosinetriphosphate by muscle proteins and its relation to muscular contraction. *J. Biol. Chem. 234*, 1102−1107.
28. Webb, M. R., and Trentham, D. R. (1981) The mechanism of ATP hydrolysis catalyzed by myosin and actomyosin, using rapid reaction techniques to study oxygen exchange. *J. Biol. Chem. 256*, 10910−10916.
29. Bowater, R., Zimmerman, R. W., and Webb, M. R. (1990) Kinetics of ATP and inorganic phosphate release during hydrolysis of ATP by rabbit skeletal actomyosin subfragment 1, Oxygen exchange between water and ATP or phosphate. *J. Biol. Chem. 265*, 171−176.
30. Kagawa, H., and Mori, K. (1999) Molecular orbital study of the interaction between MgATP and the myosin motor domain: The highest occupied molecular orbitals indicate the reaction site of ATP hydrolysis. *J. Phys. Chem. B 103*, 7346−7352.
31. Minehardt, T. J., Marzari, N., Cooke, R., Pate, E., Kollman, P. A., and Car, R. (2002) A classical and ab initio study of the interaction of the myosin triphosphate binding domain with ATP. *Biophys. J. 82*, 660−675.

BI040002M

Role of Calcineurin B Homologous Protein in pH Regulation by the Na^+/H^+ Exchanger 1: Tightly Bound Ca^{2+} Ions as Important Structural Elements†

Tianxiang Pang,‡ Takashi Hisamitsu,‡ Hidezo Mori,⊥ Munekazu Shigekawa,§ and Shigeo Wakabayashi*,‡

‡*Department of Molecular Physiology and Department of Cardiac Physiology, National Cardiovascular Center Research Institute, Suita, Osaka 565-8565, Japan, and Department of Human Life Sciences, Senri Kinran University, Suita, Osaka 565-0873, Japan*

Received November 10, 2003; Revised Manuscript Received January 27, 2004

ABSTRACT: We studied the role of the interaction of calcineurin homologous protein 1 (CHP1) with the Na^+/H^+ exchanger 1 (NHE1), particularly its EF-hand Ca^{2+} binding motifs, in the intracellular pH (pH_i)-dependent regulation of NHE1. We found that $^{45}Ca^{2+}$ binds to two EF-hand motifs (EF3 and 4) of the recombinant CHP1 proteins with high affinity (apparent K_d = ~90 nM). Complex formation between CHP1 and the CHP1 binding domain of NHE1 resulted in a marked increase in the Ca^{2+} binding affinity (K_d = ~2 nM) by promoting a conformational change of the EF-hands toward the tightly Ca^{2+}-bound form. This suggests that CHP1 always contains two Ca^{2+} ions when associated with NHE1 in cells. Interestingly, overexpression of GFP-tagged CHP1 with mutations in EF3 or EF4 significantly reduced the exchange activity in the neutral pH_i range and partly impaired the activation of NHE1 in response to various stimuli, such as growth factors and osmotic stress. Furthermore, we found that, in addition to reducing the activity (V_{max}), a CHP1 binding-defective NHE1 mutant had a marked reduction in pH_i sensitivity (~0.7 pH unit acidic shift), which consequently abolished various regulatory responses of NHE1. These observations suggest that the association of NHE1 with CHP1 is crucial for maintenance of the pH_i sensitivity of NHE1 and that tightly bound Ca^{2+} ions may serve as important structural elements in the "pH_i sensor" of NHE1.

The Na^+/H^+ exchanger (NHE1[1]) proteins in the plasma membrane and various organellar compartments of mammalian cells catalyze the electroneutral countertransport of Na^+ for H^+. Nine distinct isoforms of the Na^+/H^+ exchanger (NHE1 to NHE9) have been isolated to date, and these molecules have been shown to exhibit similar membrane topologies with 12 predicted N-terminal membrane-spanning helices and a large C-terminal cytoplasmic region (*1*−*10*). They show considerable differences in their tissue expression patterns, membrane localization, and kinetic and pharmacological properties. The plasma membrane exchangers (NHE1−5) are primarily involved in regulation of intracellular pH and Na^+ concentration, but they also participate in a broad range of physiological processes, such as cell volume regulation, transepithelial transport of electrolytes, cell proliferation, apoptosis, and differentiation (*1*−*3*).

Of the nine isoforms identified to date, NHE1 has been characterized in the most detail. NHE1 is ubiquitously expressed in essentially all tissues and cell types and plays a major role in maintaining intracellular pH and cell volume homoeostasis. The activity of NHE1 is controlled by various extrinsic factors, including growth factors, hormones, and mechanical stimuli (*1*−*3*). A variety of signaling molecules regulate the NHE1 protein, such as calcinuerin B homologous protein (CHP) (*11*−*13*), Ca^{2+}/calmodulin (*14*, *15*), the low molecular weight GTPases Ras and Rho (*16*), p42/44 mitogen-activated protein kinases (*17*), p90 ribosomal S6 kinase (*18*), 14-3-3 protein (*19*), Nck-interacting kinase (*20*), phosphatidylinositol 4,5-bisphosphate (*21*), and carbonic anhydrase II (*22*). Recently, we have focused on the role of CHP in regulation of the activities of the Na^+/H^+ exchangers (*12*, *13*).

CHP was initially discovered as a protein (p22) involved in vesicular transport (*23*), as well as a molecule that interacted with NHE (*11*). Since then, CHP has been reported

† This work was supported by Grant-in-Aid for Priority Areas 13142210 and Grant-in-Aid 14580664 for Scientific Research from the Ministry of Education, Science, and Culture of Japan, by the promotion of Fundamental Studies in Health Science of the Organization for Pharmaceutical Safety and Research of Japan (Promotion of Fundamental Studies in Health Science), and by Grant nano-001 for Research on Advanced Medical Technology from the Ministry of Health, Labor, and Welfare of Japan. T.P. was supported by a Japan Society for the Promotion of Science Postdoctoral Fellowship.

* To whom correspondence should be addressed. Department of Molecular Physiology, National Cardiovascular Center Research Institute, Fujishirodai 5-7-1, Suita, Osaka 565-8565 Japan. Tel: +81-6-6833-5012. Fax: +81-6-6835-5314. E-mail: wak@ri.ncvc.go.jp.

‡ Department of Molecular Physiology, National Cardiovascular Center Research Institute.

⊥ Department of Cardiac Physiology, National Cardiovascular Center Research Institute.

§ Senri Kinran University.

[1] Abbreviations: NHE, Na^+/H^+ exchanger; CHP, calcineurin B homologous protein; GFP, green fluorescent protein; CaN, calcineurin; CaM, calmodulin; pH_i, intracellular pH; EIPA, 5-(*N*-ethyl-*N*-isopropyl)-amiloride; DMEM, Dulbecco's modified Eagle's medium; HEPES, 2-[4-(2-hydroxyethyl)-1-piperazinyl]ethansulfonic acid; Tris, Tris(hydroxymethyl)aminomethane; EGTA, *O*,*O*′-bis(2-aminoethyl)ethylene glycol-*N*,*N*,*N*′,*N*′-tetraacetic acid; PBS, phosphate-buffered saline; PDGF-BB, platelet-derived growth factor-BB, PMA, phorbol 12-myristate 13-acetate; SDS−PAGE, sodium dodecyl sulfate−polyacrilamide gel electrophoresis.

10.1021/bi0360004 CCC: $27.50
Published on Web 03/06/2004

to exhibit multiple functions, including inhibition of calcinuerin phosphatase activity (*24*), as well as interaction with microtubules (*25*), DRAK2 (death-associated protein kinase related apoptosis inducing protein kinase 2) (*26*) and KIF1Bβ2 (kinesin-family 1Bβ2) (*27*). Previously, we reported that the ubiquitous CHP isoform (designated as CHP1) is an essential cofactor for the physiological activity of the Na^+/H^+ exchanger by interacting with the juxtamembrane region in the C-terminal cytoplasmic domain of plasma membrane exchanger isoforms (*12*). Furthermore, we reported that the second CHP isoform (CHP2) might be involved in maintenance of the abnormally high pH_i in malignantly transformed cells (*13*). CHP2 is expressed at a relatively high level in the rat small intestine (*28*), suggesting that it plays a specific role in this tissue. These CHP proteins contain four EF-hand Ca^{2+} binding motifs and are myristoylated at the N-terminus (Gly^2). In addition, CHP1 is phosphorylated in cells in a serum-dependent manner (*11*). However, the roles of these posttranslational modifications of CHP proteins in the pH_i-dependent regulation or acute activation of NHE in response to extracellular stimuli are largely unknown, although this protein family appears to be essential for the physiological exchange activity of plasma membrane NHEs.

In this study, we focused on the EF-hand Ca^{2+} binding motifs of CHP1. We found that the affinity of CHP1 for Ca^{2+} markedly (approximately 40-fold) increases upon complex formation with NHE1, probably by promoting a change in the conformation of the EF-hand motifs. The extremely low Ca^{2+} dissociation constant (~2 nM) of CHP1 suggests that Ca^{2+} ions remain tightly bound to CHP1 when it is complexed with NHE1 in the plasma membrane. On the basis of properties of various CHP1 and NHE1 mutant proteins in cells, we suggest that CHP1 is important for pH_i-dependent regulation of NHE1 and that tightly bound Ca^{2+} ions play an important role in maintaining a structure that is critical for this function of CHP1.

EXPERIMENTAL PROCEDURES

Materials. The amiloride derivative EIPA was a gift from the New Drug Research Laboratories of Kanebo, Ltd. (Osaka, Japan). $^{45}CaCl_2$, $^{22}NaCl$, and ^{14}C-benzoic acid were purchased from Dupont-NEN (Boston, MA). The rabbit polyclonal antibodies against CHP1 and NHE1 were described previously (*12*, *14*). All other chemicals were of the highest purity available.

Cells, Culture Conditions, and Stable Expression. The exchanger-deficient cell line PS120 (*29*) and corresponding transfectants were maintained in DMEM (Life Technologies Inc., Rockville, MD) containing 25 mM $NaHCO_3$ and supplemented with 7.5% (v/v) fetal calf serum, penicillin (50 units/mL), and streptomycin (50 μg/mL). Cells were maintained at 37 °C in the presence of 5% CO_2. PS120 cells (5×10^5 cells/100-mm dish) were transfected with each plasmid construct (20 μg) by the calcium phosphate coprecipitation technique. Cell populations stably expressing wild-type or mutant human NHE1 were selected by the H^+-killing procedure as described previously (*30*). Cells stably overexpressing GFP-tagged CHP1 were first selected with G418, and then single colonies were selected by monitoring GFP fluorescence.

Construction of Expression Vectors. All the constructs were produced by means of a polymerase chain reaction (PCR)-based strategy. For construction of GFP-tagged CHP1 or its mutant forms with mutations in Ca^{2+} binding motifs or in the myristoylated glycine (G2A), a cDNA encoding CHP1 was cloned into the mammalian expression vector pEGFP-N1 (Clontech, Palo Alto, CA). The plasmids carrying cDNAs for the wild-type or mutant NHE1s were all cloned into the mammalian expression vector pECE. Constructs were confirmed by sequencing plasmids with an ABI-PRISM DNA sequencer model 3100 (Applied Biosystems, Foster City, CA).

Purification of Recombinant Proteins. Recombinant histidine-tagged CHP1 proteins were produced in *Escherichia coli* (BL21-Star; Invitrogen, San Diego, CA) transformed with pET11 carrying the cDNA encoding CHP1 containing the C-terminal six histidine residues as described previously (*12*). Myristoylated CHP1 was produced using the same bacteria except they also contained the vector pBB131, which carries the yeast *N*-myristoyltransferase cDNA (kindly provided by Dr. J. I. Gordon, Washington University). Myristoylation of CHP1 (or p22) produced by this method was previously confirmed (*23*). For production of the complex of CHP1 and the CHP1 binding region of NHE1, the cytoplasmic region (aa 503−545) of NHE1 was cloned into the vector pET24 and coexpressed with His-tagged CHP1 in *E. coli* in the presence of ampicillin and kanamycin. Myristoylated and nonmyristoylated CHP1 proteins and CHP1/NHE1 (aa 503−545) complex proteins were all recovered in the soluble fraction and partially purified by passage through a Ni^{2+} affinity resin column (ProBond, Invitrogen) according to the manufacturer's protocol. Partially purified CHP1 proteins were found to be ~70% pure. We did not carry out further purification of CHP1 because of aggregation during storage. The complexes consisting of CHP1 or its mutant variants complexed with the NHE1 fragment were further purified to more than 95% by diethylaminoethyl-Sepharose column chromatography. All the proteins were dialyzed overnight against 60 mM KCl and 10 mM HEPES/Tris (pH 7.2).

Measurement of Equilibrium $^{45}Ca^{2+}$ Binding. $^{45}Ca^{2+}$ binding to the proteins was measured by a filtration method as described previously (*31*). Purified proteins (0.1−0.2 mg/mL) were incubated for 1 h at 25 °C in a solution containing 60 mM KCl, 5 mM $MgCl_2$, 50 μM $CaCl_2$, 0.02 μCi/mL $^{45}CaCl_2$, 10 mM HEPES/Tris (pH 7.2), and different concentrations of EGTA (0−58 mM), giving a free Ca^{2+} concentration of 0.1 nM to 50 μM. Aliquots (1 mL) of the reaction mixture were transferred onto 0.22-μm Millipore filters (Millipore, Bedford, MA) and filtered under vacuum. As controls, the same reaction mixtures without proteins were filtered to measure the background binding of ^{45}Ca by the filters. More than 95% of the proteins were retained in the filters. After the filters were dried, ^{45}Ca radioactivity was measured by scintillation counting.

Measurement of $^{45}Ca^{2+}$ Release from Proteins. $^{45}Ca^{2+}$ release from proteins was measured using a rapid filtration apparatus as described previously (*31*). After preincubation of proteins with a solution containing 50 μM $^{45}CaCl_2$ for 1 h, aliquots (1 mL) of reaction mixtures were filtered through Millipore filters. Filters were washed at a constant rate (0.2−2 mL/s) for the indicated periods (0.2−30 s) with

0.4−6 mL of 60 mM KCl, 5 mM $MgCl_2$, 10 mM HEPES/Tris (pH 7.2), and 10 mM EGTA. After the filters were dried, ^{45}Ca radioactivity was measured by scintilation counting.

Immunoprecipitation and Immunoblotting. Immunoprecipitation and immunoblotting were performed essentially as described previously (*14*). Briefly, cells were solubilized with 1% Triton X-100 in a solution of 150 mM NaCl, 10 mM HEPES-Tris (pH 7.4), and protease inhibitors. Cell lysates were incubated with respective antibodies and protein A Sepharose. After centrifugation, precipitated materials were separated on 7.5% or 12% polyacrylamide gels and electrophoretically transferred to Immobilon membranes (Millipore). After blocking, incubation with antibodies and washing, protein signals were visualized by enhanced chemiluminescence (Amersham, Buckinghamshire, U.K.). The signal intensity was measured using a photonic microscope system (ARUGUS-100, Hamamatsu photonics).

Measurement of $^{22}Na^+$ Uptake. $^{22}Na^+$ uptake activity and its pH_i dependence were measured by the K^+/nigericin pH_i clamp method essentially as described previously (*32*). Serum-depleted cells in 24-well dishes were incubated for 30 min at 37 °C in Na^+-free choline chloride/KCl medium containing 20 mM HEPES/Tris (pH 7.4), 1.2−140 mM KCl, 2 mM $CaCl_2$, 1 mM $MgCl_2$, 5 mM glucose (or 5 mM 2-deoxyglucose plus 2 μg/mL oligomycin under conditions of ATP depletion), and 5 μM nigericin. $^{22}Na^+$ uptake was started by adding the same choline chloride/KCl solution containing $^{22}NaCl$ (37 kBq/mL, final concentration = 1 mM), 1 mM ouabain, and 100 μM bumetanide. In some wells, 0.1 mM EIPA was added to the solution. After 1 min, cells were washed four times with ice-cold PBS to terminate $^{22}Na^+$ uptake. The pH_i was calculated from the imposed K^+ concentration gradient by assuming the equilibrium $[K^+]_i/[K^+]_o = [H^+]_o/[H^+]_i$ and an intracellular K^+ concentration of 120 mM. Data were normalized according to the protein concentration as measured by the bicinchoninic assay (Pierce Chemical Co., IL) using bovine serum albumin as a standard.

Measurement of pH_i. Changes in pH_i were measured by the [^{14}C]-benzoic acid equilibration method (*30*). For this measurement, serum-depleted cells were incubated for 30 min in bicarbonate-free HEPES-buffered DMEM (pH 7.0) and then incubated in the same medium containing [^{14}C]-benzoic acid (37 kBq/mL) for 20 min at 37 °C. After the cells were washed four times with ice-cold PBS, ^{14}C-radioactivity taken up by cells was measured. Changes in pH_i were calculated as described previously (*30*).

Statistics. Data of the pH dependence of EIPA-sensitive $^{22}Na^+$ uptake were simulated by fitting the values to the sigmoidal dose-response equation, rate of EIPA-sensitive $^{22}Na^+$ uptake = $V_{max}/(1 + 10^{\log(pK - pH_i)n})$ (pK = pH_i giving half-maximal $^{22}Na^+$ uptake; n = Hill coefficient), using the simulation program included in Graphpad Prizm (Microsoft Corp., Redmond, WA). Equilibrium $^{45}Ca^{2+}$ binding was fitted to the dose−response equation, $^{45}Ca^{2+}$ bound = maximal $^{45}Ca^{2+}$ bound/$(1 + (K_d - [Ca^{2+}])^n)$ (K_d = apparent dissociation constant for Ca^{2+}; n = Hill coefficient). Kinetic parameters were expressed as the best fit values with standard errors, whereas other data were expressed as the means ± SD for at least three determinations.

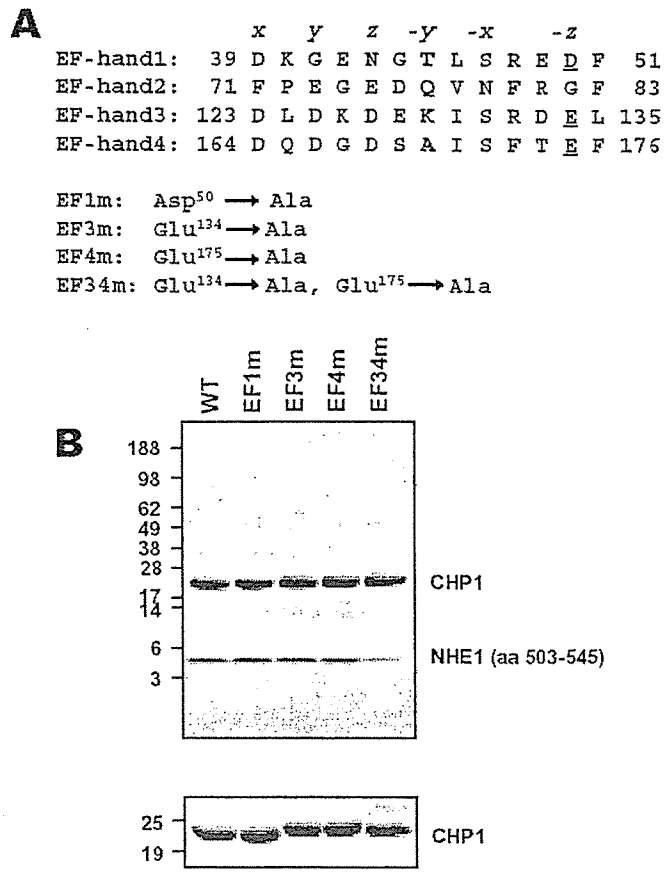

FIGURE 1: Amino acid sequences of EF-hand motifs and purified proteins of various CHP1 mutants. Panel A shows amino acid sequences of four EF-hand motifs present in CHP1. In four mutant CHP1s (EF1m, EF3m, EF4m, and EF34m), Asp^{50}, Glu^{134}, Glu^{175}, and both Glu^{134}/Glu^{175} were replaced by alanine. In panel B, the purified complex of His-tagged CHP1 with the NHE1 segment (aa 503−545) (10 μg) was separated by electrophoresis on a 4−15% gradient (upper panel) or 12% SDS−PAGE gel (lower panel) and then visualized by Coomassie Brilliant Blue staining.

RESULTS

Characterization of Ca^{2+} Binding Motifs in CHP1. We first analyzed $^{45}Ca^{2+}$ binding to EF-hand motifs of CHP1 using recombinant CHP1 and its complex with the binding domain in NHE1. CHP1 interacts with NHE1 at the juxtamembrane region of the carboxyl-terminal cytoplasmic domain of NHE1. Hydrophobic residues of NHE1, such as Phe^{526}, Leu^{527}, Leu^{530}, and Leu^{531}, were shown to be important for the interaction of CHP1 with NHE1 (*12*). CHP1 contains four potential EF-hand Ca^{2+} binding motifs, of which two ancestral sites (EF1 and -2) may not bind Ca^{2+} due to substitution of critical acidic residues (Figure 1A). The canonical EF-hand consists of 29 consecutive residues with two flanking helices and a 12-residue loop (Figure 1A). The chelating loop residues in positions 1 (+x), 3 (+y), 5 (+z), 7 (−y), 9 (−x), and 12 (−z) ligate Ca^{2+} through seven oxygen atoms arranged three-dimensionally on the axes of a pentagonal bipyramid (*33*, *34*). The −z position, providing the only side chain oxygen atoms, is crucial for Ca^{2+} binding (*33*−*35*). To characterize these Ca^{2+} binding motifs, we introduced mutations into EF1, -3, and -4 in which acidic residues (aspartic acid or glutamic acid) at the −z position were replaced by alanine (Figure 1B). We coexpressed the wild-type or mutant CHP1s together with the juxtamembrane region of NHE1 (aa 503−545) in *E. coli*. We confirmed that

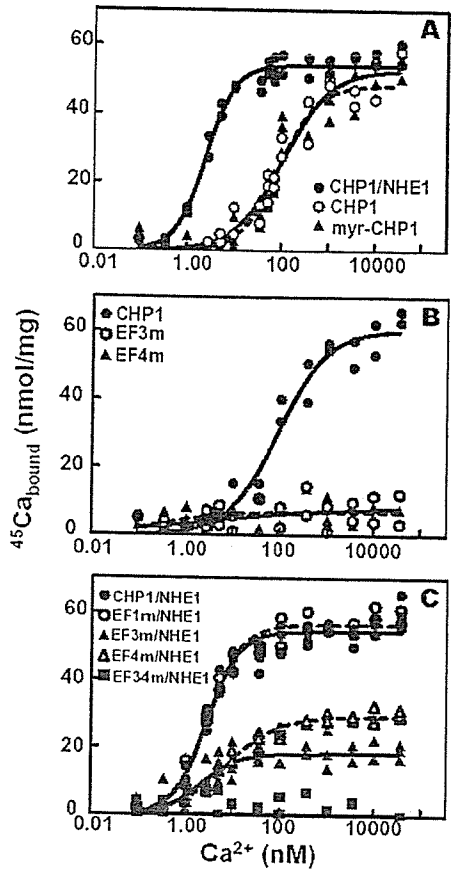

FIGURE 2: Equilibrium $^{45}Ca^{2+}$ binding to various CHP1 mutant proteins. In panels A–C, CHP1 or its various mutant proteins and the complex of CHP1 variants with the NHE1 segment (aa 503–545) (0.1–0.2 mg/mL) were incubated for 1 h in solutions containing 50 μM $^{45}CaCl_2$ and various concentrations of EGTA, which produce 0.2 nM to 50 μM free Ca^{2+}. Symbols corresponding to each protein variant were indicated in figures. The solutions were filtered through Millipore filters, and $^{45}Ca^{2+}$ bound to the CHP1 proteins was measured.

the purified complex proteins (>95% pure) of the wild-type CHP1, EF1m, EF3m, or EF4m with aa 503–545 of NHE1 were retained as a single peak on gel filtration chromatography and contained the CHP1 variant and the NHE1 peptide at a 1:1 molar ratio (data not shown). In addition, using 4–15% polyacrylamide gradient gels, we confirmed that the purified samples mostly contained comparable molar amounts of the CHP1 variant and the NHE1 fragment (Figure 1B, upper panel). However, in EF34m with double mutations at EF3 and -4, the amount of the NHE1 fragment was significantly reduced, suggesting that this double mutation impairs the interaction of CHP1 with NHE1. On 12% SDS–PAGE, EF3m, EF4m, and EF34m proteins were found to migrate more slowly than the wild-type or EF1m proteins (Figure 1B, lower panel), suggesting that a mutation-induced conformational change occurred in these three mutant proteins that had impaired Ca^{2+} binding (see below).

We measured $^{45}Ca^{2+}$ binding to various CHP1 mutant proteins by a membrane filtration procedure. We found that $^{45}Ca^{2+}$ bound to the partially purified CHP1 proteins with an apparent K_d of ~90 nM (Figure 2A and Table 1). The maximal amount of $^{45}Ca^{2+}$ bound to CHP1 corresponded to ~2 mol of Ca^{2+} bound/mol of CHP1, assuming that the CHP1 sample was 70% pure. Myristoylation did not significantly affect the apparent affinity for Ca^{2+} nor the

Table 1: Parameters for Equilibrium $^{45}Ca^{2+}$ Binding

proteins	apparent K_d ± SE (nM)[a]	Hill coefficient ± SE
CHP1	89.9 ± 9.3	0.77 ± 0.12
myr-CHP1	86.4 ± 8.9	0.94 ± 0.17
CHP1/NHE1	2.32 ± 0.18	1.22 ± 0.15
EF1m/NHE1	2.17 ± 0.39	0.98 ± 0.14
EF3m/NHE1	2.89 ± 0.28	1.27 ± 0.55
EF4m/NHE1	2.24 ± 0.26	0.76 ± 0.09

[a] The data shown in Figure 2 were fitted to the equation for equilibrium $^{45}Ca^{2+}$ binding as described in Experimental Procedures.

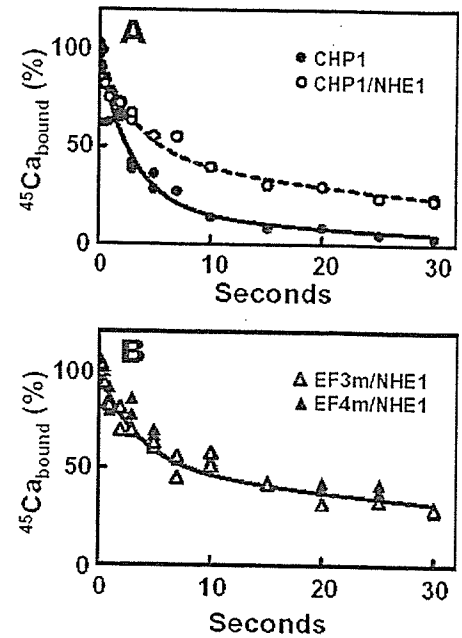

FIGURE 3: Time courses of $^{45}Ca^{2+}$ release from CHP1 proteins: (A) $^{45}Ca^{2+}$ release from CHP1 alone (●) or CHP1/NHE1 complex (○); (B) $^{45}Ca^{2+}$ release from EF3m/NHE1 (△) or EF4m/NHE1 complex (▲). CHP1 proteins or the complex of CHP1 variants with the NHE1 segment (aa 503–545) (0.1–0.2 mg/mL) were incubated for 1 h in a solution containing 50 μM $^{45}CaCl_2$, applied to Millipore filters, and washed with a solution containing EGTA. $^{45}Ca^{2+}$ remaining on the filters was measured.

maximal level of $^{45}Ca^{2+}$ binding (Figure 2A and Table 1). Interestingly, when CHP1 formed a complex with the NHE1 fragment, the binding affinity for $^{45}Ca^{2+}$ increased markedly (~40-fold, Figure 2A and Table 1). The extremely low apparent dissociation constant (~2 nM) deviates substantially from the physiological cytosolic Ca^{2+} concentration of cells (0.1–10 μM). The maximal level of Ca^{2+} binding on the complex again corresponded to ~2 mol of Ca^{2+} bound/mol of CHP1. Mutation of either of Ca^{2+} binding motifs EF3 or EF4, but not EF1, resulted in loss of approximately 1 mol of $^{45}Ca^{2+}$ bound to the complex (Figure 2C). On the other hand, $^{45}Ca^{2+}$ binding was completely blocked when the experiment was carried out using EF3m and EF4m proteins but without the NHE1 fragment (Figure 2B) or when two sites were simultaneously mutated (EF34m) (Figure 2C). Together, these results indicate that CHP1 binds two Ca^{2+} ions, one at EF3 and the other at EF4.

To determine how complex formation increases the Ca^{2+} binding affinity, we measured $^{45}Ca^{2+}$ release from CHP1 proteins by rapid filtration. As shown in Figure 3A, most of the $^{45}Ca^{2+}$ bound to CHP1 without the NHE1 fragment was released rapidly ($t_{1/2}$ = ~2 s). In contrast, $^{45}Ca^{2+}$ release from

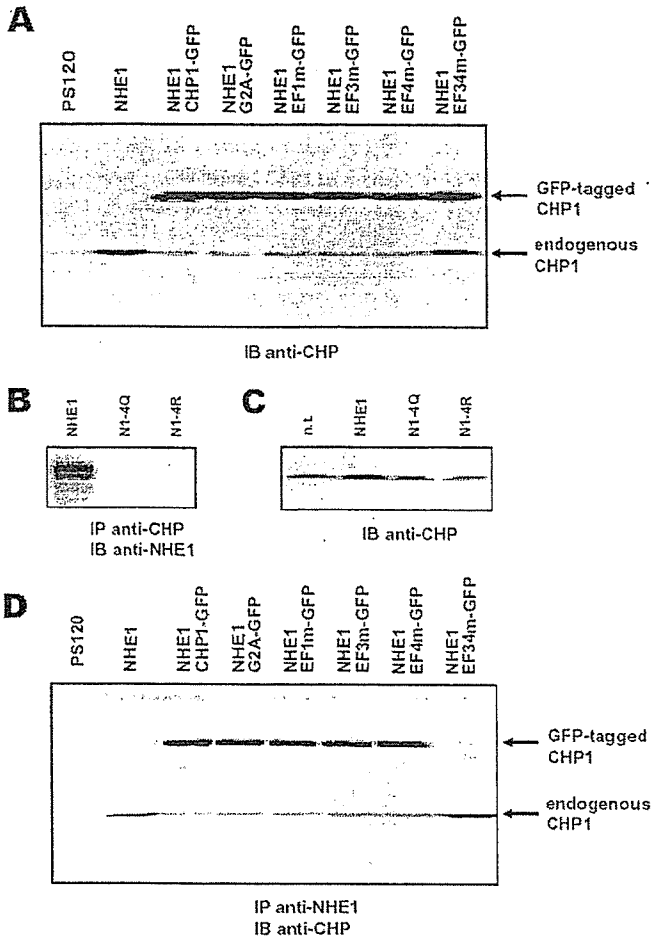

FIGURE 4: Expression of various GFP-tagged CHP1 proteins and their coimmunoprecipitation with NHE1. Panel A shows the expression level of GFP-tagged CHP1 and its variants (indicated at the top of the figure). Cell lysates (50 μg) from stable transfectants were subjected to SDS−PAGE, and expression of endogenous and exogenous CHP1 proteins were detected by immunoblotting (IB) with an anti-CHP1 antibody. A result for untransfected PS120 cells is shown in the first lane. Panel B shows coimmunoprecipitation of the wild-type or mutant (4Q and 4R) exchangers with endogenous CHP1. Lysates from cells stably expressing these exchangers were subjected to immunoprecipitation with anti-CHP1 antibody followed by immunoblotting with anti-NHE1 antibody. Panel C shows the expression level of endogenous CHP1 in cells expressing the wild-type or mutant NHE1s: n.t., no transfection. Panel D shows coimmunoprecipitation of CHP1 proteins with NHE1. Lysates from cells stably expressing various proteins were subjected to immunoprecipitation with anti-NHE1 antibody followed by immunoblotting with anti-CHP1 antibody. Note that in lanes from cells not transfected with GFP-tagged CHP1 (left two lanes), IgG protein bands were visible at the same positions as GFP-tagged CHP1.

CHP1 complexed with the NHE1 fragment ($t_{1/2} = \sim 7$ s) was much slower. A slow release of $^{45}Ca^{2+}$ also occurred in two mutant CHP1 proteins, EF3m and EF4m, complexed with the NHE1 fragment (Figure 3B), suggesting that Ca^{2+} binds tightly to each EF hand.

Effects of CHP1 Mutations on NHE1 Regulation. To study the role of Ca^{2+} binding in NHE1 regulation by CHP1, we transfected GFP-tagged CHP1 into cells expressing NHE1 and obtained cells stably coexpressing these proteins. The results indicated that GFP-tagged CHP1 and its mutant derivatives were highly coexpressed in NHE1 transfectants (Figure 4A). Interestingly, expression of NHE1 markedly increased the level of expression of the endogenous CHP1 (3.6-fold), while coexpression of various GFP-tagged CHP1 variants, with the exception of CHP1-EF34m-GFP, reduced it (Table 2).

Table 2: Relative Amounts of Expressed GFP-Tagged CHP1 and Endogenous CHP1

transfected proteins	relative amount of GFP-tagged CHP1[a]	relative amount of endogenous CHP[b]
untransfected		1.00 ± 0.08
NHE1		3.63 ± 0.81[c]
NHE1 + CHP1-GFP	1.00 ± 0.11	1.11 ± 0.13
NHE1 + G2A-GFP	1.08 ± 0.11	1.03 ± 0.16
NHE1 + EF1m-GFP	0.93 ± 0.06	1.07 ± 0.11
NHE1 + EF3m-GFP	0.97 ± 0.11	1.15 ± 0.16
NHE1 + EF4m-GFP	1.06 ± 0.07	1.09 ± 0.10
NHE1 + EF34m-GFP	0.94 ± 0.12	3.85 ± 0.45[c]
NHE1-4Q		1.02 ± 0.09
NHE1-4R		1.03 ± 0.06

[a] The density of visualized protein bands on immunoblots (cf. Figure 4, panels A and C) is represented as values normalized according to the band density from cells expressing CHP1-GFP. Data are means ± SD ($n = 3$). [b] The band density is represented as values normalized according that from untransfected PS120 cells. Data are means ± SD ($n = 3$). [c] $P < 0.05$ versus control.

We further examined the effect of expression of CHP1 binding-defective NHE1 mutants 4Q and 4R on the amount of endogenous CHP. These mutant exchangers do not bind CHP1 as shown by coimmunoprecipitation studies (Figure 4B). The level of expression of the endogenous CHP1 did not increase on coexpression of these mutant exchangers (Figure 4B,C, Table 2). Thus, the amount of endogenous CHP1 in cells is highly dependent on expression of NHE1 and GFP-tagged CHP1.

Figure 4D shows the results for coimmunoprecipitation experiments using NHE1- and CHP1-specific antibodies to determine interactions of the expressed CHP1−GFP with NHE1. Anti-NHE1 antibody immunoprecipitated endogenous CHP1 from cells expressing NHE1. In cells coexpressing GFP−CHP1 and NHE1, the same antibody coimmunoprecipitated large quantities of GFP−CHP1 or its derivatives, and at the same time, the amount of immunoprecipitated endogenous CHP1 was markedly reduced. In cells coexpressing EF34m−GFP and NHE1, anti-NHE1 antibody coimmunoprecipitated the endogenous CHP1 but not exogenous GFP-tagged mutant CHP1, consistent with the findings of in vitro binding studies indicating that double mutation at EF3 and EF4 impairs the interaction of CHP1 with NHE1.

We next examined the subcellular localization of GFP-tagged CHP1. As reported previously (*12*), the GFP-tagged CHP1 is localized in the plasma membrane in cells coexpressing NHE1 (Figure 5A). Consistent with the in vitro binding data (Figure 1B), the GFP fluorescence was observed in the plasma membrane in cells coexpressing GFP-tagged CHP1 mutants except EF34m with NHE1 (Figure 5A; data not shown for G2A and EF1m). These results, together with the data from coimmunoprecipitation experiments, indicate that the endogenous CHP1 bound to NHE1 was efficiently replaced by expressed GFP-tagged wild-type or CHP1 mutants. However, the double mutant EF34m was not localized at the plasma membrane (Figure 5A) because of the weak interaction of this mutant protein with the juxtamembrane region of NHE1. We observed that GFP fluorescence was still observed in the plasma membrane after addition of phorbol ester, serum, thrombin, lysophosphatidic

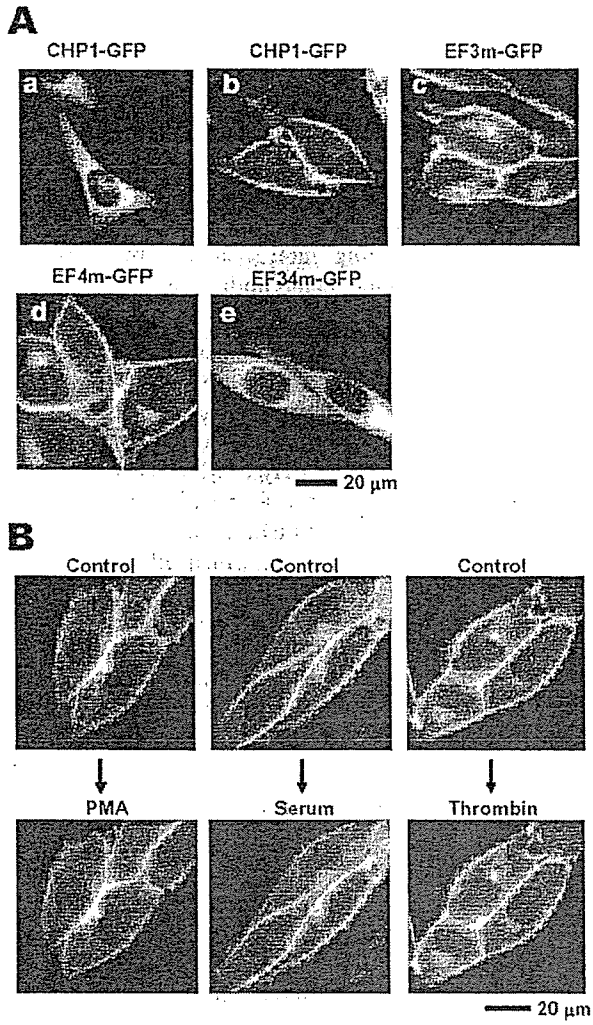

FIGURE 5: Subcellular localization of GFP-tagged CHP1: (A) subcellular localization of GFP-tagged wild-type CHP1 (a, b), EF3m (c), EF4m (d), and EF34m (e) expressed in PS120 cells (a) or in their stable transfectants of the wild-type NHE1 (b–e); (B) effect of various agents on the subcellular localization of the wild-type GFP-tagged CHP1 in NHE1 transfectants. Cells were placed in serum-free Dulbecco's modified Eagle's medium without phenol red for 5 h, and then 1 μM PMA, 10% serum, or 2 units/ml thrombin were added. GFP fluorescence was observed under a fluorescent microscope equipped with a CoolSNAP imaging system (RS Photometrics) before (control) and 20 min after addition of the various agents.

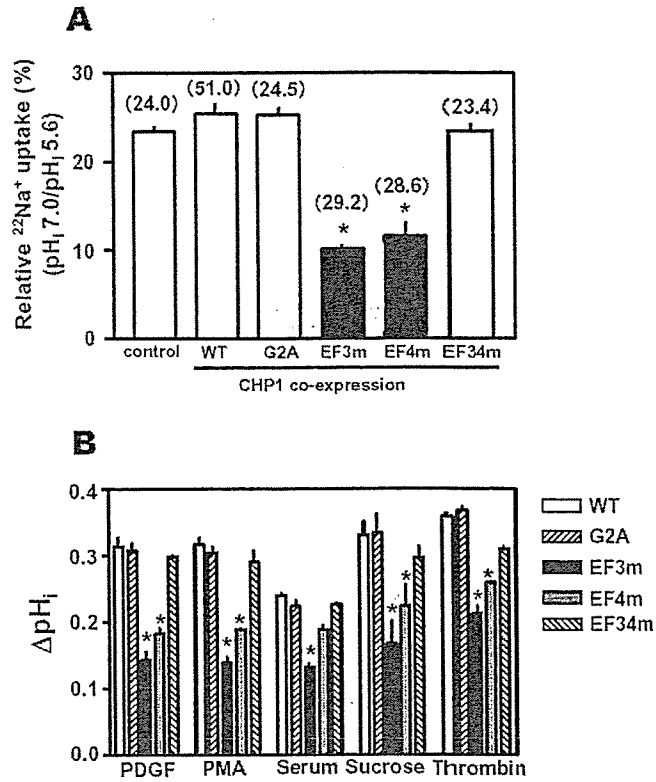

FIGURE 6: Exchange activity and regulation of NHE1 transfectants expressing various CHP1 mutants. Panel A shows ratios of EIPA-sensitive $^{22}Na^+$ uptake activities of cells coexpressing wild-type NHE1 and various CHP1 mutants at pH_i 7.0 and 5.6. Numbers (nmol/mg/min) in parentheses represent $^{22}Na^+$ uptake activity at pH_i = 5.6. Control cells were not transfected with CHP1 but stably expressing NHE1. Data are means ± SD (n = 3; *, P < 0.05 versus cells not expressing exogenous CHP1). Panel B shows changes in pH_i measured using the [^{14}C]benzoic acid equilibration method. The cells coexpressing NHE1 and various CHP1 variants were stimulated for 15 min at 37 °C with 10 ng/mL PDGF-BB, 1 μM PMA, 10 μg/mL lysophosphatidic acid, or 200 mM sucrose (hyperosmotic stress). Data are means ± SD (n = 6; *, P < 0.05 versus cells expressing wild-type CHP1).

acid, or PDGF-BB, which are all known to activate the exchange activity (Figure 5B, data not shown for some experiments). We also found that the plasma membrane localization of GFP fluorescence did not change upon addition of metabolic inhibitors (2-deoxyglucose plus oligomycin) that cause cell ATP depletion, thus inhibiting exchange activity (data not shown). Furthermore, we found no changes in the plasma membrane localization of GFP-tagged CHP1 mutants EF3m and EF4m after these various treatments (data not shown). These observations suggest that CHP1 is tightly associated with NHE1 in the plasma membrane and that this interaction is not affected by various stimuli.

All the cells expressing CHP1–GFP or its mutant derivatives exhibited high Na^+/H^+ exchange activity. The $^{22}Na^+$ uptake activity in cells clamped at acidic pH_i (5.6) by the K^+/nigericin technique was in the range of 20–50 nmol/mg/min (data not shown). We compared the $^{22}Na^+$ uptake activities in cells expressing various CHP1 variants in the physiological pH_i range. As shown in Figure 6A, the ratio of $^{22}Na^+$ uptake at pH_i 7.2–5.6 was not significantly altered by expression of wild-type CHP1. Although a previous study (*11*) indicated that overexpression of CHP1 inhibits the NHE1 activity in the presence of serum, we observed no such CHP1-induced inhibition of the exchange activity. The reason for this discrepancy is unknown. Unlike the wild-type CHP1, the $^{22}Na^+$ uptake ratio was significantly reduced by EF3 or EF4 mutants. Consistent with this finding, we observed that mutations of EF3 or EF4 significantly reduced the cytoplasmic alkalinization in response to PDGF-BB, thrombin, phorbol ester, serum, or hyperosmotic stress (sucrose) (Figure 6B). These observations suggest that mutation of EF3 or EF4 partly impairs the regulation of NHE1 by reducing pH_i sensitivity. In contrast, double mutation (EF34m) of CHP1 at EF3 and EF4 did not reduce the $^{22}Na^+$ uptake ratio or cytoplasmic alkalinization (Figure 6A,B), consistent with the finding that this mutant CHP1 is not able to replace the endogenous CHP1 because of its weak interaction with NHE1. Finally, mutation of the myristoylation site (G2A) or EF1 did not affect pH_i-dependent regulation of NHE1.

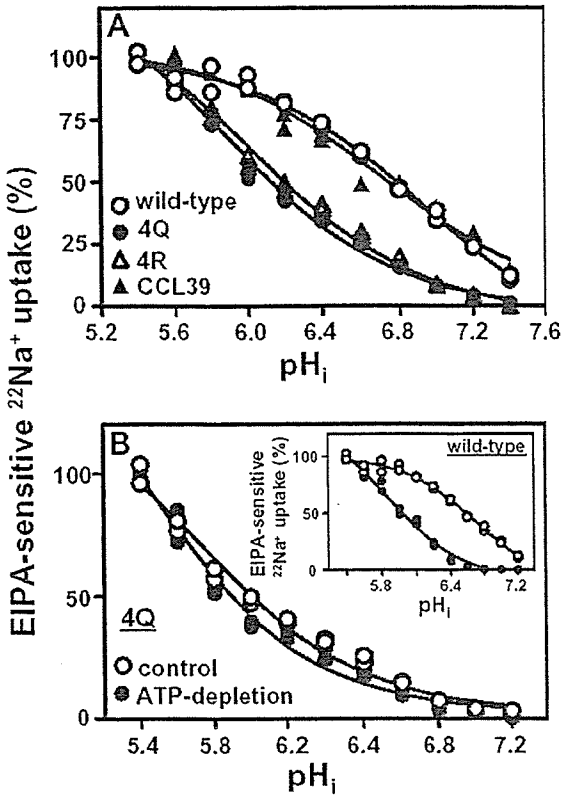

FIGURE 7: pH_i dependence of exchange activity in cells expressing some NHE variants. Panel A shows the pH_i dependence of $^{22}Na^+$ uptake in PS120 cells expressing wild-type NHE1 or CHP1 binding-defective mutants 4Q and 4R and CCL39 fibroblastic cells (the parental cell line of PS120). pH_i was clamped at various values with K^+/nigericin. The maximal EIPA-sensitive $^{22}Na^+$ uptake activity measured at $pH_i = 5.4$ was high in cells expressing wild-type NHE1 (~50 nmol/mg/min), while it was lower but similar in cells expressing 4Q or 4R or in CCL39 cells (4.2, 4.2, or 4.1 nmol/mg/min, respectively). Data were normalized according to the maximal activity at $pH_i = 5.4$. Panel B shows the effects of ATP depletion on pH_i dependence of exchange activity in cells expressing 4Q or wild-type NHE1 (inset). Cells were depleted of ATP by treatment with the metabolic inhibitors 2-deoxyglucose (5 mM) and oligomycin (2 μg/mL). Data were normalized according to the maximal activity at $pH_i = 5.4$.

Properties of NHE1 Mutants Lacking CHP1 Binding. As described above, mutations of CHP1 partly impair pH_i-dependent regulation of NHE1. Therefore, it is of interest to determine how CHP1 binding affects the pH_i sensitivity of NHE1. Previously, we described two CHP1 binding-defective mutant exchangers, 4Q or 4R, in which Phe^{526}, Leu^{527}, Leu^{530}, and Leu^{531} of NHE1 were replaced by four glutamine or arginine residues, respectively (*12*) (see Figure 4B). In this study, by using extensive H^+-killing selection, we obtained cells overexpressing 4Q or 4R and exhibiting relatively high activity (~4 nmol/mg/min at pH_i 5.4), thus allowing reliable measurement of the pH_i dependence of $^{22}Na^+$ uptake. As shown in Figure 7A, these mutations caused a marked acidic shift in the pH_i dependence (Figure 7A). As a control, we confirmed that CCL39 cells (the parental cell line of PS120) that exhibit exchange activity (V_{max}) comparable to 4Q or 4R show a pH_i dependence of exchange similar to that of PS120 cells overexpressing NHE1. In cells expressing these mutant exchangers, ATP depletion did not change the pH_i sensitivity of $^{22}Na^+$ uptake (Figure 7B). In addition, cytoplasmic alkalinization in response to extracellular stimuli, such as thrombin, PDGF-BB, hyperosmolarity, LPA, and PMA, was not observed in cells expressing 4Q or 4R (data not shown), consistent with the finding that these mutants exhibit an acidic shift of pH_i dependence.

DISCUSSION

In this study, we examined the role of CHP1, particularly its EF-hand Ca^{2+} binding motifs, in the pH_i-dependent regulation of NHE1. Our results indicated that a Ca^{2+} ion binds to each of EF3 and EF4 in CHP1 with an overall apparent K_d of ~90 nM and a Hill coefficient of ~1.0 (Table 1). This Ca^{2+} binding affinity was close to that of another family member, CaN-B (apparent $K_d \approx 70$ nM) (*36*), although the apparent K_d values for Ca^{2+} in other EF-hand Ca^{2+} binding proteins vary widely (0.01−10 μM) (*36*−*39*). Although CHP1 potentially has four Ca^{2+} binding motifs, the two ancestral sites EF1 and EF2 do not bind Ca^{2+}. This is in sharp contrast to CaN-B in which all four EF-hand motifs are able to bind Ca^{2+}, although the two N-terminal sites, EF1 and EF2, have lower affinity for Ca^{2+} than the C-terminal sites, EF3 and EF4 (*36*). Intriguingly, the Ca^{2+} affinity of CHP1 increased markedly upon complex formation with the NHE1 fragment (aa 503−545). Consistent with this finding, $^{45}Ca^{2+}$ release from the complex was much slower than that from CHP1 alone. The extraordinarily high affinity of CHP1 for Ca^{2+} (~2 nM) suggests that the CHP1/NHE1 complex always contains two Ca^{2+} ions under physiological conditions.

The high affinity for Ca^{2+} was also observed in mutant CHP1 proteins EF3m and EF4m, which have a single Ca^{2+} binding site, complexed with the NHE1 fragment. Increases in the affinity for Ca^{2+} by interaction with target proteins have also been reported for other Ca^{2+} binding proteins. For example, the Ca^{2+} binding affinity for calmodulin was increased 16- to 38-fold upon interaction with myosin light chain kinase (*40*), 2.6-fold with myristoylated alanine-rich protein kinase C substrate peptide (*41*), and 75-fold with the calmodulin binding peptide in CaN-A (*36*). CHP1 was reported to interact with other proteins, such as microtubules (*25*), CaN-A (*24*), DRAK2 (*26*), and KIF1Bβ2 (*27*), as well as members of the NHE1 family. Therefore, interaction with these proteins may also modify the Ca^{2+} binding affinity of CHP1.

Although mutation of CHP1 at either EF3 or EF4 impaired binding of 1 mol of Ca^{2+}, it did not appear to affect the interaction of CHP1 with NHE1 as shown by in vitro binding of these mutant proteins, coimmunoprecipitation, and the plasma membrane localization of GFP-tagged CHP1. Therefore, these mutations do not appear to induce marked structural distortions. However, double mutation (EF34m) at both EF3 and EF4 impaired the interaction of CHP1 with NHE1. Consistent with this finding, Ca^{2+} removal by EGTA from the wild-type CHP1 reduced the interaction with NHE1 in a pull-down assay through the amyrose resin column (data not shown). Thus, the tight association of NHE1 with CHP1 requires binding of at least one Ca^{2+} on either EF3 or EF4. Furthermore, it should be noted that the effect of double mutation (EF34m) on regulation of NHE1 cannot be properly analyzed in cells that express endogenous CHP1.

We found that expression of NHE1, but not the CHP1 binding-deficient mutant derivatives 4Q and 4R, significantly

increased the amount of endogenous CHP1. However, coexpression of GFP-tagged CHP1 proteins (wild-type, EF3m, and EF4m) preserving the strong interaction with NHE1 greatly reduced the amount of endogenous CHP1. Thus, the amount of endogenous CHP1 in cells is strongly dependent on the number of available CHP1 binding sites provided from NHE1. Although the precise reason for this is unknown, it is likely that interaction with target proteins is required for stable expression of CHP1. That is, dissociation from the target proteins may promote CHP1 degradation.

In this study, we found that CHP1 binding-defective mutants of NHE1 (4Q and 4R) caused a marked acidic shift in the pH_i dependence of Na^+/H^+ exchange activity and completely impaired ATP depletion-induced inhibition and cytoplasmic alkalinization in response to various stimuli. As we reported previously (*32*), not only mutation of the CHP1 binding region, but also deletions of different regions in the amino-terminus (subdomain I, amino acids 515−595) of the NHE1 cytoplasmic domain also markedly reduced pH_i sensitivity. Thus, subdomain I with bound CHP1 appears to be a key structure that permits the putative "pH-sensor" to maintain a physiologically relevant conformation.

We found that mutation of EF3 or EF4 in CHP1 significantly reduced the Na^+/H^+ exchange activity in the physiological neutral pH_i range and reduced the cytoplasmic alkalinization in response to various extracellular signals by decreasing the pH_i sensitivity of NHE1. Thus, mutation of each EF-hand in CHP1 somehow affects the pH_i-sensing of NHE1, although we could not evaluate the function of the double mutant CHP1 (EF34m) because of its weak interaction with NHE1. We found that EF3m, EF4m, and EF34m proteins migrated slowly on SDS−PAGE, suggesting that significant conformational changes of CHP1 occur upon mutation of each EF-hand. Such conformational changes appear to be due to removal of Ca^{2+} rather than the amino acid substitution itself, because incubation with EGTA resulted in similar slow migration of the wild-type CHP1 on SDS−PAGE (data not shown). Thus, the bound Ca^{2+} may play an important role in maintaining the CHP1 structure, thereby preserving the physiological pH_i sensitivity of NHE1.

According to the structural model of CHP1 deduced from the three-dimensional structure of CaN-B (*43*), EF-hand Ca^{2+} binding motifs would be located on the surface opposite the side where CHP1 binds to NHE1. It is likely that the surface of CHP1 with tightly bound Ca^{2+} controls the pH_i-sensing by interacting with other region(s) of NHE1. We observed that the pH_i sensitivity of NHE1 was markedly reduced by insertion of one amino acid residue (alanine) just to the N-terminal side (position aa 504 or 508) of the CHP1 binding site of NHE1, while the CHP1 binding ability was preserved (our unpublished observations). Therefore, the correct spatial orientation of CHP1 would be important for regulation of NHE. Recently, we reported that mutation of Arg^{440} in intracellular loop 5 (IL5), which connects transmembrane helices 10 and 11, markedly reduces the pH_i sensitivity of NHE1 (*44*). Thus, IL5 may interact with the CHP1 surface with tightly bound Ca^{2+}.

Many EF-hand Ca^{2+} binding proteins are known to regulate the functions of their target proteins in response to cytosolic Ca^{2+} mobilization. However, it is unlikely that CHP1 functions as such a Ca^{2+} sensor in the regulation of NHE1 because the affinity for Ca^{2+} ($K_d = \sim 2$ nM) for the CHP1/NHE1 complex differs substantially from the range of intracellular Ca^{2+} concentrations (0.1−10 μM). Instead, two EF-hand motifs of CHP1 together with tightly bound Ca^{2+} would serve as structurally important elements for preserving the normal function of NHE1, as discussed above. Such a structural role has also been suggested in the C-terminal EF-hand motifs in CaN-B (*42*) and in CaM (*41*). On the other hand, we reported previously that CaM interacts in a Ca^{2+}-dependent manner with the middle of the cytoplasmic domain of NHE1, which in the unstipulated state serves as an auto inhibitory domain decreasing the pH_i sensitivity of NHE1 (*14*, *15*). The interaction of NHE1 with CaM is strictly Ca^{2+}-dependent, although it is much weaker than that with CHP1 (*14*). Previously, we proposed that NHE1 may be activated by Ca^{2+}-dependent interaction of CaM in response to Ca^{2+}-mobilizing signals (*15*). Our previous (*14*, *15*) and several recent reports (*45*−*48*) reinforced the idea that CaM serves as an important regulatory protein in activation of NHE1 in response to hyperosmotic stress or Ca^{2+}-mobilizing agonists. NHE1 thus appears to be dually regulated by two Ca^{2+} binding proteins, CHP1 and CaM, similar to CaN-A. The former would preserve the physiological pH_i sensitivity of NHE1, whereas the latter would play a role in sensing cytosolic Ca^{2+}.

In summary, our current results suggest that the interaction of CHP1 with NHE1 is crucial for preserving the physiological pH_i sensitivity of NHE1 and that tightly bound Ca^{2+} serves as an important structural element that is required for this role. The significant effects of mutations in EF-hands on NHE1 regulation prompted us to generate a more efficient dominant negative mutant CHP1. In addition, the functional difference between CHP1 and CHP2, which we reported recently (*13*), provides important information for identification of the critical residues of CHP1. Further studies including analyses of the functions of mutated or chimerical CHP1 and determination of the crystal structure of CHP1/NHE1 complex are required to elucidate the molecular mechanism of CHP regulation of NHE1 and other NHE family members.

REFERENCES

1. Wakabayashi, S., Shigekawa, M., and Pouysségur, J. (1997) Molecular physiology of vertebrate Na^+/H^+ exchangers, *Physiol. Rev. 77*, 51−74.
2. Orlowski, J., and Grinstein, S. (1997) Na^+/H^+ exchangers of mammalian cells, *J. Biol. Chem. 272*, 22373−22376.
3. Counillon, L., and Pouysségur, J. (2000) The expanding family of eucaryotic Na^+/H^+ exchangers, *J. Biol. Chem. 275*, 1−4.
4. Sardet, C., Franchi, A., and Pouysségur, J. (1989) Molecular cloning, primary structure, and expression of the human growth factor-activatable Na^+/H^+ antiporter, *Cell 56*, 271−280.
5. Orlowski, J., Kandasamy, R. A., and Shull, G. E., (1992) Molecular cloning of putative members of the Na/H exchanger gene family, *J. Biol. Chem. 267*, 9331−9339.
6. Tsé, C.-M., Brant, S. R. Walker, M. S., Pouysségur, J., and Donowitz, M. (1992) Cloning and sequencing of a rabbit cDNA encoding and intestinal and kidney-specific Na^+/H^+ exchanger isoform (NHE-3), *J. Biol. Chem, 267*, 9340−9346.
7. Numata, M., Petrecca, K., Lake, N., and Orlowski, J. (1998) Identification of a mitochondrial Na^+/H^+ exchanger, *J. Biol. Chem. 273*, 6951−6959.
8. Numata, M., and Orlowski, J. (2001) Molecular cloning and characterization of a novel (Na^+, K^+)/H^+ exchanger localized to the *trans*-Golgi network, *J. Biol. Chem. 276*, 17387−17394.
9. Baird, N., Orlowski, J., Szabo, E. Z., Zaun, H. Schultheis, P. J., Menon, A. G., and Shull, G. (1999) Molecular cloning, genomic

organization, and functional expression of Na^+/H^+ exchanger isoform 5 (NHE5) from human brain, *J. Biol. Chem. 274*, 4377−4382.

10. Goyal, S., Vanden Heuvel, G., and Aronson, P. S. (2003) Renal expression of novel Na^+/H^+ exchanger isoform NHE8, *Am. J. Physiol. 284*, F467−473.
11. Lin, X., and Barber, D. L. (1996) A calcineurin homologous protein inhibits GTPase-stimulated Na−H exchange, *Proc. Natl. Acad. Sci. U.S.A. 93*, 12631−12636.
12. Pang, T., Su, X., Wakabayashi, S., and Shigekawa, M. (2001) Calcineurin homologous protein as an essential cofactor for Na^+/H^+ exchangers, *J. Biol. Chem. 276*, 17367−17372.
13. Pang, T., Wakabayashi, S., and Shigekawa, M. (2002) Expression of calcineuin B homologous protein 2 protects serum deprivaion-induced cell death by serum-independent activation of Na^+/H^+ exchanger, *J. Biol. Chem. 277*, 43771−43777.
14. Bertrand, B., Wakabayashi, S., Ikeda, T., Pouysségur, J., and Shigekawa, M. (1994) The Na^+/H^+ exchanger isoform 1 (NHE1) is a novel member of the calmodulin-binding proteins: Identification and characterization of calmodulin-binding sites, *J. Biol. Chem. 269*, 13703−13709.
15. Wakabayashi, S., Bertrand, B., Ikeda, T., Pouysségur, J., and Shigekawa, M. (1994) Mutation of calmodulin-binding site renders the Na^+/H^+ exchanger (NHE1) highly H^+-sensitive and Ca^{2+} regulation-defective, *J. Biol. Chem. 269*, 13710−13715.
16. Voyno-Yasenetskaya, T., Conklin, B. R., Gilbert, R. L., Hooley, R., Bourne, H. R., and Barber, D. L. (1994) G alpha 13 stimulates Na−H exchange, *J. Biol. Chem. 269*, 4721−4724.
17. Bianchini, L., L'Allemain, G., and Pouysségur, J. (1997) The p42/p44 Mitogen-activated protein kinase cascade is determinant in mediating activation of the Na^+/H^+ exchanger (NHE1 isoform) in response to growth factors, *J. Biol. Chem. 272*, 271−279.
18. Takahashi, E., Abe, J.-I., Gallis, B., Aebersold, R., Spring, D. J., Krebs, E. G., and Berk, B. C. (1999) $p90^{RSK}$ is a serum-stimulated Na^+/H^+ exchanger isoform-1 kinase. Regulatory phosphorylation of serine 703 of Na^+/H^+ exchanger isoform-1, *J. Biol. Chem. 274*, 20206−20214.
19. Lehoux, S., Abe, J. I., Florian, J. A., and Berk, B. C. (2001) 14-3-3 binding to Na^+/H^+ exchanger isoform-1 is associated with serum-dependent activation of Na^+/H^+ exchange, *J. Biol. Chem. 276*, 15794−15800.
20. Yan, W., Nehrke, K., Choi, J., and Barber, D. L. (2001) The Nck-interacting kinase (NIK) phosphorylates the Na^+-H^+ exchanger NHE1 and regulates NHE1 activation by platelet-derived growth factor, *J. Biol. Chem. 276*, 31349−31356.
21. Aharonovitz, O., Zaun, H. C., Balla, T., York, J. D., Orlowski, J., and Grinstein, S. (2000) Intracellular pH regulation by Na^+/H^+ exchange requires phosphatidylinositol 4,5-bisphosphate, *J. Cell Biol. 150*, 213−224.
22. Li, X., Alvarez, B., Casey, J. R., Reithmeier, R. A. F., and Fliegel, L. (2002) Carbionic anhydrase II binds to and enhances activity of the Na^+/H^+ exchanger, *J. Biol. Chem. 277*, 36085−36091.
23. Barroso, M. R., Bernd, K. K., DeWitt, N. D., Chang, A., Mills, K., and Sztul, E. S. (1996) A novel Ca^{2+}-binding protein, p22, is required for constitutive membrane traffic, *J. Biol. Chem. 271*, 10183−10187.
24. Lin, X., Sikkink, R. A., Rusnak, F., and Barber, D. L. (1999) Inhibition of calcineurin phosphatase activity by a calcineurin B homologous protein, *J. Biol. Chem. 274*, 36125−36131.
25. Timm, S., Titus, B., Bernd, K., and Barroso, M. (1999) The EF-hand Ca^{2+}-binding protein p22 associates with microtubules in an N-myristoylation-dependent manner, *Mol. Biol. Cell 10*, 3473−3488.
26. Matsumoto, M., Miyake, Y., Nagita, M., Inoue, H., Shitakubo, D., Takemoto, K., Ohtsuka, C., Murakami, H., Nakamura, N., and Kanazawa, H. (2001) A serine/threonine kinase which causes apoptosis-like cell death interacts with a calcineurin B-like protein capable of binding Na^+/H^+ exchanger, *J. Biochem. (Tokyo) 130*, 217−225.
27. Nakamura, N., Miyake, Y., Matsushita, M., Tanaka, S., Inoue, H., and Kanazawa, H. (2002) KIF1Bβ2, capable of interacting with CHP, is localized to synaptic vesicles, *J. Biochem. (Tokyo) 132*, 483−492.
28. Inoue, H., Nakamura, Y., Nagita, M., Takai, T., Masuda, M., Nakamura, N., and Kanazawa, H. (2003) Calcineurin homologous protein isoform 2 (CHP2), Na^+/H^+ exchangers-binding protein, is expressed in intestinal epithelium, *Biol. Pharm. Bull. 26* (2), 148−155.
29. Pouysségur, J., Sardet, C., Franchi, A., L'Allemain, G., and Paris, S. (1984) A specific mutation abolishing Na^+/H^+ antiport activity in hamster fibroblasts precludes growth at nertral and acidic pH, *Proc. Natl. Acad. Sci. U.S.A. 81*, 4833−4837.
30. Wakabayashi, S., Fafournoux, P., Sardet, C., and Pouysségur, J. (1992) The Na^+/H^+ antiporter cytoplasmic domain mediates growth factor signals and controls "H^+-sensing", *Proc. Natl. Acad. Sci. U.S.A. 89*, 2424−2428.
31. Wakabayashi, S., Ogurusu, T., and Shigekawa, M. (1986) Factors influencing calcium release from the ADP-sensitive phosphoenzyme intermediate of the sarcoplasmic reticulum ATPase, *J. Biol. Chem. 261*, 9762−9769.
32. Ikeda, T., Schmitt, B., Pouysségur, J., Wakabayashi, S., and Shigekawa, M. (1997) Identification of cytoplasmic subdomains that control pH-sensing of theNa^+/H^+ exchanger (NHE1): pH-maintenance, ATP-sensitive, and flexible loop domains, *J. Biochem. (Tokyo) 121*, 295−303.
33. Strynadka, N. C. J., and James, M. N. G. (1989) Crystal structures of the helix-loop-helix calcium-binding proteins, *Annu. Rev. Biochem. 58*, 951−998.
34. Yap, K. L., Ames, J. B., Swindells, M. B., and Ikura, M. (1999) Diversity of conformational states and changes within the EF-hand protein superfamily, *Proteins 37*, 499−507.
35. Szebenyi, D. M. E., Obendorf, S. K., and Moffat, K. (1981) Structure of vitamin D-dependent calcium-binding protein from bovine intestine, *Nature 294*, 327−332.
36. Stemmer, P. M., and Klee, C. B. (1994) Dual Calcium Ion Regulation of Calcineurin by Calmodulin and Calcineurin B, *Biochemistry 33*, 6859−6866.
37. Pauls, T. L., Durussel, I., Cox, J. A., Clark, I. D., Szabo, A. G., Gagne, S. M., Sykes, B. D., and Berchtold, M. W. (1993) Metal binding properties of recombinant rat parvalbumin wild-type and F102W mutant, *J. Biol. Chem. 268*, 20897−20903.
38. Gross, M. D., Gosnell, M., Tsarbopoulos, A., and Hunziker, W. (1993) A functional and degenerate pair of EF hands contains the very high affinity calcium-binding site of calbindin-D_{28K}, *J. Biol. Chem. 268*, 20917−20992.
39. Burgoyne, R. D., and Weiss, J. L. (2001) The neuronal calcium sensor family of Ca^{2+}-binding proteins, *Biochem. J. 353*, 1−12.
40. Olwin, B. B., Edelman, A. M., Krebs, E. G., and Storm, D. R. (1984) Quantitation of energy coupling between Ca^{2+}, calmodulin, skeletal muscle myosin light chain kinase, and kinase substrates, *J. Biol. Chem. 259*, 10949−10955.
41. Johnson, J. D., Snyder, C., Walsh, M., and Flynn, M. (1996) Effects of myosin light chain kinase and peptides on Ca^{2+} exchange with the N- and C-terminal Ca^{2+} binding sites of calmodulin, *J. Biol. Chem. 271*, 761−767.
42. Feng, B., and Stemmer, P. M. (1999) Interactions of calcineurin A, calcineurin B, and Ca^{2+}, *J. Biol. Chem. 38*, 12481−12489.
43. Kissinger, C. R., Parge, H. E., Knighton, D. R., Lewis, C. T., Pelletier, L. A., Tempczyk, A., Kalish, V. J., Tucker, K. D., Showalter, R. E., Moomaw, E. W., Gastinel, L. N., Habuka, N., Chen, X., Maldonado, F., Barker, J. E., Bacquet, R., and Villafranca, J. E. (1995) Crystal structures of human calcineurin and the human FKBP12−FK506-calcineurin complex, *Nature 378*, 641−644.
44. Wakabayashi, S., Hisamitsu, T., Pang, T., and Shigekawa, M. (2003) Mutations of Arg^{440} and Gly^{455}/Gly^{456} oppositely change pH sensing of Na^+/H^+ exchanger 1, *J. Biol. Chem. 278*, 11828−11835.
45. Garnovaskaya, M. N., Mukhin, Y. V., Vlasova, T. M., and Raymond, J. R. (2003) Hypertonicity activates Na^+/H^+ exchange through Janus kinase 2 and calmodulin, *J. Biol. Chem. 278*, 16908−16915.
46. Mukhin, Y. V., Vlasova, T., Jaffa, A. A., Collinsworth, G., Bell, J. L., Tholanikunnel, B. G., Petus, T., Fitzgibbon, W., Ploth, D. W., Raymond, J. R., and Garnovskaya, M. N. (2001) Bradykinin B_2 receptors activate Na^+/H^+ exchange in mIMCD-3 cells via Janus kinase 2 and Ca^{2+}/calmodulin, *J. Biol. Chem. 276*, 17339−17346.
47. Robertson, M. A., Woodside, M., Foskett, J. K., Orlowski, J., and Grinstein, S. (1997) Muscarinic agonists induce phosphorylation-independent activation of the NHE−1 isoform of the Na^+/H^+ antiporter in salivary acinar cells, *J. Biol. Chem. 272*, 287−294.
48. Moor, AN, Murtazina, R, and Fliegel, L. (2000) Calcium and osmotic regulation of the Na^+/H^+ exchanger in neonatal ventricular myocytes, *J. Mol. Cell. Cardiol. 32*, 925−936.

BI0360004

In Situ Measurements of Crossbridge Dynamics and Lattice Spacing in Rat Hearts by X-Ray Diffraction

Sensitivity to Regional Ischemia

James T. Pearson, PhD; Mikiyasu Shirai, MD, PhD; Haruo Ito, PhD; Noriyuki Tokunaga, MD; Hirotsugu Tsuchimochi, PhD; Naoki Nishiura; Daryl O. Schwenke, PhD; Hatsue Ishibashi-Ueda, MD; Ryuichi Akiyama, PhD; Hidezo Mori, MD, PhD; Kenji Kangawa, PhD; Hiroyuki Suga, MD, PhD; Naoto Yagi, PhD

Background—Synchrotron radiation has been used to analyze crossbridge dynamics in isolated papillary muscle and excised perfused hearts with the use of x-ray diffraction techniques. We showed that these techniques can detect regional changes in rat left ventricle contractility and myosin lattice spacing in in situ ejecting hearts in real time. Furthermore, we examined the sensitivity of these indexes to regional ischemia.

Methods and Results—The left ventricular free wall of spontaneously beating rat hearts (heart rate, 290 to 404 bpm) was directly exposed to brief high-flux, low-emittance x-ray beams provided at SPring-8. Myosin mass transfer to actin filaments was determined as the decrease in reflection intensity ratio (intensity of 1,0 plane over the 1,1 plane) between end-diastole and end-systole. The distance between 1,0 reflections was converted to a lattice spacing between myosin filaments. We found that mass transfer (mean, 1.71±0.09 SEM, n=13 hearts) preceded significant increases in lattice spacing (2 to 5 nm) during systole in nonischemic pericardium. Left coronary occlusion eliminated increases in lattice spacing and severely reduced mass transfer ($P<0.01$) in the ischemic region.

Conclusions—Our results suggest that x-ray diffraction techniques permit real-time in situ analysis of regional crossbridge dynamics at molecular and fiber levels that might also facilitate investigations of ventricular output regulation by the Frank-Starling mechanism. **(*Circulation*. 2004;109:2976-2979.)**

Key Words: ischemia ■ myocardial contraction ■ myosin ■ radiography

Despite the history of studies on crossbridge dynamics, lower photon counts and poorer quality of diffraction patterns obtained from cardiac muscle than skeletal and insect flight muscles[1–3] have limited progress with cardiac muscle until recently.[4,5] Some of us used third-generation synchrotron radiation (SPring-8, Japan Synchrotron Radiation Research Institute) to determine x-ray diffraction patterns in excised, perfused rat hearts while moving systematically across the left ventricular (LV) equator from the epicardium through to the ventricular cavity.[6]

X-ray diffraction patterns of cardiac muscle produce 2 equatorial-position reflections from the lattice-like arrangement of its protein elements.[2] Mass transfer of myosin heads to actin during contraction is inferred from a decrease in the integrated 1,0 reflection intensity ($I_{1,0}$, lattice plane containing only thick myosin filaments) and an increase in 1,1 reflection intensity ($I_{1,1}$, plane with thick myosin and thin actin filaments).[7] The myocardial intensity ratio (defined as $I_{1,0}/I_{1,1}$) is minimal in the rigor state and maximal in a quiescent state.[1,2,6,8]

Furthermore, the distance between 1,0 reflection peaks ($d_{1,0}$ spacing) represents the myosin lattice spacing, which is inversely related to sarcomere length in isolated fibers[5] as static myocytes maintain a constant cell volume. Whether decreases in myofilament spacing contribute to increasing Ca^{2+} sensitivity and increased probability of crossbridge formation at longer sarcomere lengths has been actively debated.[9] However, it is still not known if lattice spacing is regulated to maintain constant lattice volume (ie, if lattice cross-sectional area decreases with increasing sarcomere length, then interfilament spacing must decrease) during dynamic contractions in vivo.

Recently, it was shown that the intensity ratio derived from x-ray diffraction patterns of isolated whole hearts decreased during isovolumic contractions with a similar time course throughout the LV,[6] implying that crossbridge cycling in fibers of different myocardial layers is similar despite differences in fiber orientation and rate of short-

Received March 1, 2004; de novo received March 31, 2004; revision received May 6, 2004; accepted May 6, 2004.

From the National Cardiovascular Center Research Institute, Osaka, Japan (J.T.P., M.S., N.T., H.T., N.N., D.O.S., H.I.-U., H.M., K.K., H.S.); S-I Medico-Tech Co Ltd, Kashiwara, Osaka, Japan (H.I.); Muroran Institute of Technology, Muroran, Japan (R.A.); and SPring-8/JASRI, Sayo, Hyogo, Japan (N.Y.)

Correspondence to Dr James T. Pearson, Cardiac Physiology, National Cardiovascular Center Research Institute, 5-7-1 Fujishirodai, Suita, Osaka 565-8565 Japan. E-mail jpearson@ri.ncvc.go.jp

Circulation is available at http://www.circulationaha.org

DOI: 10.1161/01.CIR.0000133322.19340.EF

ening. However, it was not possible to follow dynamic lattice spacing changes. In the present study, we used a fine-focused x-ray beam to record diffraction patterns of a localized region of the LV of ejecting rat hearts in situ and then determined crossbridge cycling and myosin lattice spacing.

Methods

Animals and Surgical Preparation

Anesthetized (50 mg/kg sodium pentobarbital IP) male Sprague-Dawley rats (Japan SLC, Hamamatsu, Japan), 9 to 10 weeks of age (350 to 400 g), were artificially ventilated and thoractomized. Procedures were performed according to SPring-8 guidelines for the care and welfare of experimental animals. The heart was continuously irrigated while the apex was raised by a manipulator paddle and restrained by 2 superficial sutures in the LV to minimize vertical movements. Pressure-volume loops were recorded from an apically inserted 1.4F micromanometer (SPR-671 Millar Instruments) and a 1.5F conductance catheter (S-I Medico-tech Co Ltd, Osaka)[10] to determine the temporal sequence of cardiac events and heart rate (determined from end-diastole [ED] interval).

X-Ray Diffraction With Collimated Synchrotron Radiation

Measurements were conducted at the 40XU beamline of SPring-8.[6] A collimated quasimonochromatic beam (wavelength, 0.08 nm) with a beam flux of $\approx 10^{12}$ photons per second (15 keV; ring current, 60 to 100 mA) and dimensions 0.2 × 0.2 mm was focused at an oblique tangent to the myocardium ($\approx$3 m from the detector). The ventilator was stopped at end-expiration to reduce heart movements during measurements ($\approx$2.1 seconds). Images were digitally recorded at a 15-ms sampling interval with the use of an image intensifier and a fast CCD camera,[6] simultaneous with pressure-volume analog signals (1000-Hz sampling frequency). The beam passed through the apical myocardium between the ends of the descending branch of the left coronary artery (LAD) and the posterior interventricular vein. Final burning of the recorded region (higher energy levels) confirmed that the beam only exposed fibers in the epicardium and part of the intermediate layer (histological inspection).

Acute Ischemia Treatment

Heart baseline recordings were established, permanent ligation of the proximal LAD was performed, and recordings were repeated 5 to 10 minutes later.

Intensity Ratio Calculations and Analyses

Integrated intensity of $I_{1,0}$ and $I_{1,1}$ was determined from the areas under the reflection peaks after background subtraction.[6] Intensity ratio ($I_{1,0}/I_{1,1}$) was used rather than absolute reflection intensities of $I_{1,0}$ and $I_{1,1}$, which are influenced by changes in the quantity of fibers sampled during contractions.[3] Myosin mass transfer index was defined as the difference in intensity ratio between ED and end systole (ES).

Results

Mass Transfer and Lattice Spacing in Nonischemic Hearts

Intensity ratio significantly decreased during systole (increase in LV pressure [LVP] and decrease in LV volume [LVV]) and conversely, increased during diastole under the baseline rhythm (Figure 1a). Averaging intensity ratio over multiple beats reduced variability during diastole in the otherwise sinusoidal patterns (black lines, Figure 1b). With regard to time, $d_{1,0}$ spacing increased continuously

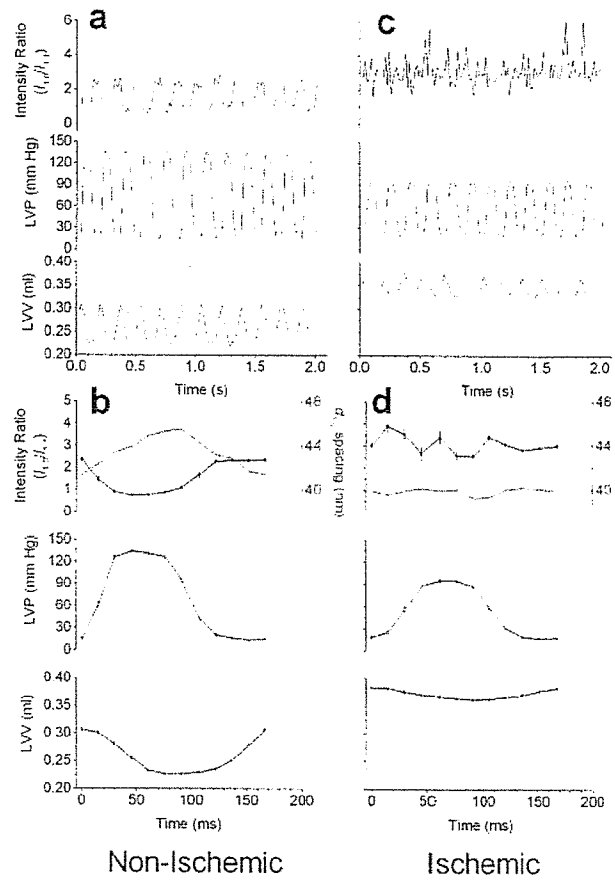

Figure 1. Relations between calculated intensity ratio, $d_{1,0}$ spacing, LVP, and LVV obtained from an LV with the use of x-ray diffraction. a and c, Consecutive records (15-ms intervals) of intensity ratio, LVP, and LVV during the baseline (a) and after LAD occlusion (c) in the same heart. b and d, Average changes in intensity ratio (black lines), $d_{1,0}$ spacing (red lines), LVP, and LVV over the cardiac cycle between the ED events (derived from a and c, respectively; bars indicate SEM).

during systole and then decreased during diastole, suggesting that considerable changes occur in the myofilament spacing (red line, Figure 1b).

Intensity ratio averaged 2.80±0.11 (SEM, n=13 hearts) at ED, and the average myosin mass transfer index was 1.71±0.09. In all hearts, the decrease in intensity ratio during crossbridge formation was completed before the full extent of the $d_{1,0}$ spacing change (2 to 5 nm between hearts, Figure 2a). Furthermore, at any given LVV, the $d_{1,0}$ spacing during systole was 1 to 2 nm larger than diastole (Figure 2b).

Mass Transfer and Lattice Spacing During Regional Ischemia

LAD occlusion reduced the intensity ratio change and prevented normal lattice spacing increase, consistent with reduced contractility of the ischemic region (Figure 1, c and d). Occlusion significantly increased intensity ratios at both ED ($P<0.05$) and ES ($P<0.001$) in the same LV region (n=6,

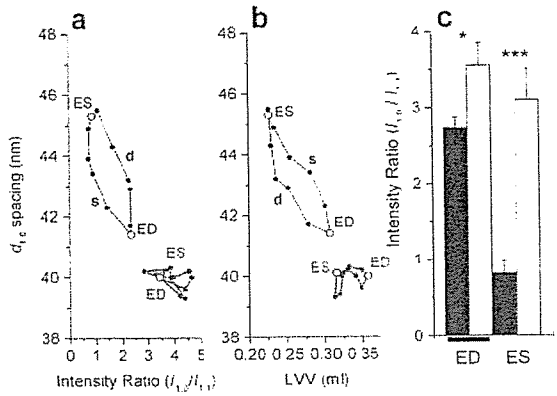

Figure 2. a and b, Average loops formed between $d_{1,0}$ spacing, LVV, and intensity ratio during consecutive cycles (shown in Figure 1) under baseline conditions (black symbols) and regional ischemia (red symbols). Systolic (s) and diastolic (d) trajectories are indicated for baseline. c, Mean intensity ratio at ED and ES during baseline (black columns) and regional ischemia (open columns; group mean±SEM). Ischemia versus baseline, paired *t* test $^{*}P<0.05$, $^{***}P<0.001$.

Figure 2c). Although mean heart rate was not depressed (341±16 bpm, 4% increase) and there was only a small decrease in mean LV ES pressure (−26.9±5.8 mm Hg SEM), regional ischemia severely depressed the mass transfer index (55% of baseline).

Discussion

Our data clearly demonstrate that current synchrotron technology can produce sufficient energy to obtain well-defined reflections from single exposures to enable calculation of intensity ratio and $d_{1,0}$ spacing in in situ rat hearts (Figure 1). The mean ED intensity ratio of this study is similar to 2.96 obtained from LV in arrested rat hearts under normoxic perfusion.[8] Furthermore, in rat papillary muscles, the resting ratio was 3.07.[1,2] The results presented here were restricted to epicardial recordings (within 0.8-mm depth), consisting of helically orientated fibers, to minimize the contributions from fibers with orientations that vary at greater depth.[11] Nevertheless, it was recently established that neither diastolic intensity ratio nor mass transfer varies with depth of x-ray beam penetration in beating, perfused hearts (paced at 2 Hz).[6]

In Situ Changes in Myofilament Spacing

We showed that significant lattice expansion occurs during contraction and that the relation between $d_{1,0}$ spacing and intensity ratio is not linear but a loop in nonischemic hearts (black line, Figure 2a). The $d_{1,0}$ spacing changes during contraction (2 to 5 nm) were larger than the 1-nm difference in $d_{1,0}$ spacing reported between the epicardium and endocardium (at diastole).[6] Therefore, the larger $d_{1,0}$ spacing change found in ejecting hearts cannot be explained by shifts in the fiber layers exposed to the beam. The loop formed by these indexes might contain valuable information about how crossbridge axial and radial forces alter the dynamics of lattice spacing changes. Crossbridge projections from the myosin backbone produce radial force perpendicular to that of axial force in the filament direction.[12] Release of isometric tension in intact skeletal myofibers during sarcomere shortening causes a brief and rapid lattice spacing increase, in excess of that predicted by fiber shortening in itself.[12,13] We therefore conclude that lattice volume is not constant in the dynamic state because myosin lattice spacing is significantly larger (1 to 2 nm) during contraction than ventricular filling at the same LVV ($d_{1,0}$ spacing during systole greater than diastole, Figure 2b). Crossbridge formation probably causes a brief lattice expansion in ejecting hearts mediated by radial forces.

Sensitivity of In Situ Indexes to Regional Ischemia

The relevance of our new findings is that although the intensity ratio of beating hearts in diastole was similar to that of relaxed papillary muscles, there is a very different response of the myocardium in beating hearts to ischemia in terms of crossbridge dynamics and lattice space changes. Higher intensity ratios and more variable intensity ratio changes during systole (Figure 1, c and d) occurred as the result of lower absolute $I_{1,1}$ in systole and a lack of consistent increase in $I_{1,1}$ when $I_{1,0}$ decreased (data not shown). Thus, permanent regional ischemia severely attenuated mass transfer in the epicardium (Figure 2c). Furthermore, ischemia induced increases in ED intensity ratio in vivo, whereas other studies report maximal decreases in the intensity ratio under anoxic perfusion (isolated arrested hearts)[8] or rigor.[1,2] An increase in intensity ratio might be related to metabolite accumulation or pronounced passive stretching, because fiber shortening in infarcted regions progressively decreases until fibers eventually become passively stretched (bulging) by fiber shortening in the nonischemic region.[14] In support of the bulging possibility, we found that $d_{1,0}$ spacing no longer increases between ED and ES after occlusion.

The cellular basis of the Frank-Starling law of the heart involves increases in contractility caused by length-dependent increases in Ca^{2+} sensitivity associated with increased ventricular filling.[9] However, it is still debated whether increased crossbridge activation results from increased probability of crossbridge formation with decreasing lattice spacing associated with fiber stretching (see review in Reference 9). In a future publication, we will examine how LV volume loading influences mass transfer in relation to myofilament spacing and length-dependent activation of contraction in situ.

Acknowledgments

This work was supported by the Promotion of Fundamental Studies in Health Sciences of the Organization for Pharmaceutical Safety and Research (OPSR) and Ministerial grants Nano-001 and a Grant-in-Aid for Scientific Research. The experiments were made with approval of the SPring-8 Program Review Committee. We thank Dr Keiji Umetani for access to the Medical Imaging Center.

References

1. Matsubara I, Kamiyama A, Suga H. X-ray diffraction study of contracting heart muscle. *J Mol Biol*. 1977;111:121–128.
2. Matsubara I, Suga H, Yagi N. An X-ray diffraction study of the cross-circulated canine heart. *J Physiol (London)*. 1977;270:311–320.

3. Yagi N, Saeki Y, Ishikawa T, et al. Cross-bridge and calcium behavior in ferret papillary muscle in different thyroid states. *Jpn J Physiol*. 2001;51:319–326.
4. Konhilas JP, Irving TC, de Tombe PP. Myofilament calcium sensitivity in skinned rat cardiac trabeculae: role of interfilament spacing. *Circ Res*. 2002;90:59–65.
5. Irving TC, Konhilas J, Perry D, et al. Myofilament lattice spacing as a function of sarcomere length in isolated rat myocardium. *Am J Physiol*. 2000;279:H2568–H2573.
6. Yagi N, Shimizu J, Mohri S, et al. X-ray diffraction from a left ventricular wall of rat heart. *Biophys J*. 2004;86:2286–2294.
7. Huxley HE, Brown W. The low-angle x-ray diagram of vertebrate striated muscle and its behaviour during contraction and rigor. *J Mol Biol*. 1967;30:383–434.
8. Sowerby AJ, Harries J, Diakun GP, et al. X-ray diffraction studies of whole rat heart during anoxic perfusion. *Biochem Biophys Res Commun*. 1994;202:1244–1251.
9. Konhilas JP, Irving TC, de Tombe PP. Frank-Starling law of the heart and the cellular mechanisms of length-dependent activation. *Pflugers Arch*. 2002;445:305–310.
10. Ito H, Takaki M, Yamaguchi H, et al. Left ventricular volumetric conductance catheter for rats. *Am J Physiol*. 1996;270:H1509–H1514.
11. Streeter DD Jr, Spotnitz HM, Patel DP, et al. Fiber orientation in the canine left ventricle during diastole and systole. *Circ Res*. 1969;24:339–347.
12. Cecchi G, Bagni MA, Griffiths PJ, et al. Detection of radial cross-bridge force by lattice spacing changes in intact single muscle fibers. *Science*. 1990;250:1409–1411.
13. Bagni M, Cecchi G, Griffiths P, et al. Lattice spacing changes accompanying isometric tension development in intact single muscle fibers. *Biophys J*. 1994;67:1965–1975.
14. Lew WYW, Chen Z, Guth B, et al. Mechanisms of augmented segment shortening in nonischemic areas during acute ischemia of the canine left ventricle. *Circ Res*. 1985;56:351–358.

研　究　論　文

Monochromatic polycapillary imaging utilizing a computed radiography system

Michiaki Sagae[1)*], Eiichi Sato[1)], Yasuomi Hayasi[1)], Etsuro Tanaka[2)], Hidezo Mori[3)], Toshiaki Kawai[4)], Haruo Obara[5)], Toshio Ichimaru[6)], Kazuyoshi Takayama[7)], Hideaki Ido[8)]

[1)] *Department of Physics, Iwate Medical University*
[2)] *Department of Nutritional Science, Faculty of Applied Bio-science, Tokyo University of Agriculture*
[3)] *Department of Cardiac Physiology, National Cardiovascular Center Research Institute*
[4)] *Electron Tube Division #2, Hamamatsu Photonics Inc.*
[5)] *Department of Radiological Technology, College of Medical Science, Tohoku University*
[6)] *Department of Radiological Technology, School of Health Sciences, Hirosaki University*
[7)] *Shock Wave Research Center, Institute of Fluid Science, Tohoku University*
[8)] *Department of Applied Physics and Informatics, Faculty of Engineering, Tohoku Gakuin University*

Research Code No.: 200, 204.1
Key Words: monochromatic radiography, quasi-parallel radiography, x-ray lens, polycapillary plate

Abstract

A fundamental study on quasi-parallel radiography using a polycapillary plate and a copper-target x-ray tube is described. In the experiments, the tube voltage was regulated from 12 to 22 kV, and the tube current was regulated within 3.0 mA by the filament temperature. The exposure time was controlled in order to obtain optimum x-ray intensity, and the maximum focal spot dimensions were approximately 2.0 × 1.5 mm. The thickness and the inner capillary tube diameter of the polycapillary were 1.0 mm and 25 μm, respectively. Monochromatic x-rays were produced using a 10 μm-thick nickel filter with a tube voltage of 17 kV, and these rays were formed into quasi-parallel beams by the polycapillary. The radiogram was taken using a computed

* 岩手医科大学教養部物理学科〔〒020-0015 岩手県盛岡市本町通3-16-1〕: Department of Physics, Iwate Medical University
e-mail: msagae@iwate-med.ac.jp

radiography system utilizing imaging plates. In the measurement of image resolution, the spatial resolution hardly varied according to increases in the distance between the resolution-test chart and imaging plate using a polycapillary. A 50 μm tungsten wire could be observed, and fine blood vessels of approximately 100 μm were visible in angiography.

Received Jan. 7, 2004; revision accepted Jul. 5, 2004

1. Introduction

Monochromatic parallel radiography typically utilizes a synchrotron in conjunction with silicon single crystals and it has been applied in x-ray phase imaging[1-3]. It has also been applied in high contrast micro-angiography[4-7] because x-rays with energies of approximately 35 keV are absorbed effectively by the iodine-based contrast medium.

In order to produce monochromatic x-rays without using the synchrotron, we developed a molybdenum x-ray tube[8] with a transmission-type molybdenum target, which is used as a monochromatic filter for absorbing bremsstrahlung x-rays. In addition, from weakly ionized linear plasma, we found irradiations of intense and sharp characteristic x-rays[9-12].

Recently, several different x-ray lenses[13,14] have been developed, and a polycapillary plate[8-15] has been shown to be useful to perform quasi-parallel radiography with lower photon energy. For this, the plate thickness is about 1 mm, and it is very difficult to design a thicker plate due to technical limitation for increasing the strait capillary length.

In biomedical radiography, because the image processing can be done easily with a Computed Radiography (CR) system[16,17] utilizing imaging plates, the CR system is useful for monochromatic parallel radiography, regardless of whether the image resolution falls as compared with an x-ray film; the spatial resolution is primarily determined by the minimum sampling pitch of 87.5 μm.

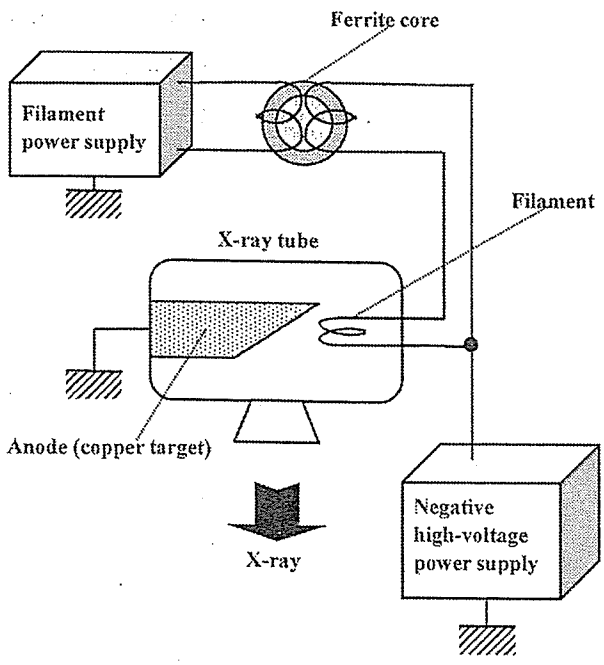

Fig. 1. Circuit diagram of the x-ray generator.

In this article, we describe a monochromatic quasi-parallel radiography system utilizing a polycapillary plate with an inner capilliary diameter of 25 μm, a CR system, and a copper-target radiation tube to realize a low-priced x-ray system utilizing an x-ray lens.

2. Experimental setup

Figure 1 shows the circuit diagram of the x-ray generator, which consists of a negative high-voltage power supply, a filament (hot cathode) power supply, and a copper-target x-ray tube. The negative high voltage is applied to the cathode electrode, and the anode (target) is connected to the ground. In the experiments, the

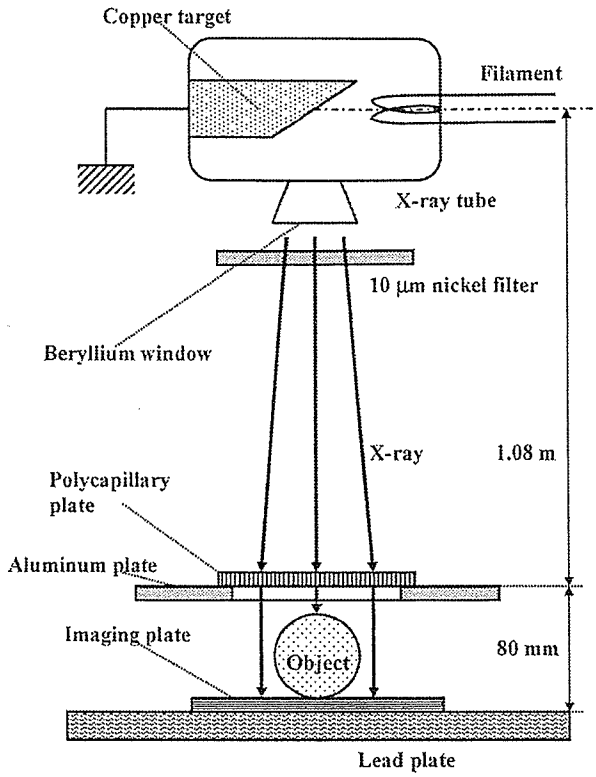

Fig. 2. Experimental setup for polycapillary imaging utilizing a CR system.

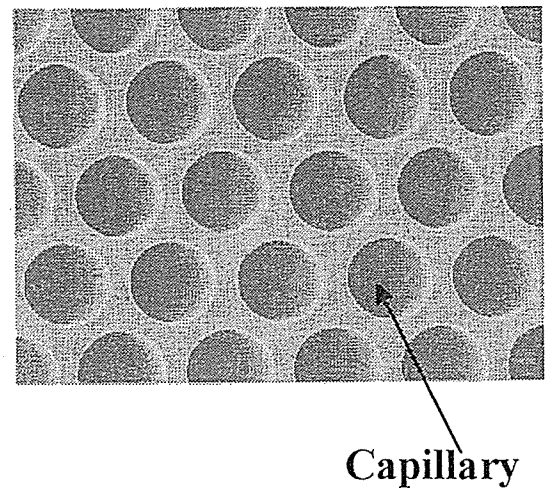

Fig. 3. Polycapillary plate.

tube voltage was regulated from 12 to 22 kV, and the tube current was regulated by the filament temperature and ranged from 1.0 to 3.0 mA. The exposure time was controlled in order to obtain optimum x-ray intensity.

The experimental setup for performing polycapillary imaging is shown in Fig. 2. Monochromatic x-rays were produced using a 10 μm-thick nickel filter, and these rays were formed into quasi-parallel beams by a polycapillary plate (Fig. 3). The polycapillary plate was J5022-21 (Hamamatsu Photonics Inc.), and the plate thickness was 1.0 mm. The outer, effective, and inner capilliary diameters were 87 mm, 77 mm, and 25 μm, respectively. Radiography was performed by a CR system (Konica Regius 150) utilizing imaging plates. The distance between the x-ray source and the polycapillary was 1.08 m, and the polycapillary plate was set on an aluminum plate. The distance between the polycapillary and imaging plates was regulated by the height (30 mm) of the polymethyl methacrylate (PMMA) spacers used.

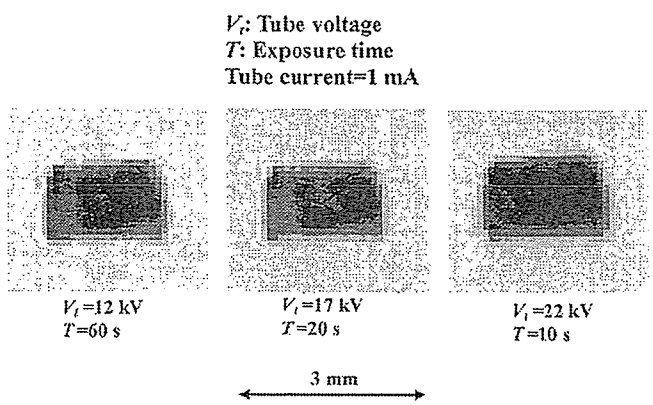

Fig. 4. Images of the x-ray source measured using a 50 μm-diameter pinhole while changing the tube voltage.

3. Characteristics

3.1. Focal spot

In order to measure images of the x-ray source, we employed the CR system, a pinhole camera with a hole diameter of 50 μm, and a filter (Fig. 4). When the tube voltage was increased, the focal spot intensity increased; spot dimensions also increased slightly and were approximately 2.0 × 1.5 mm.

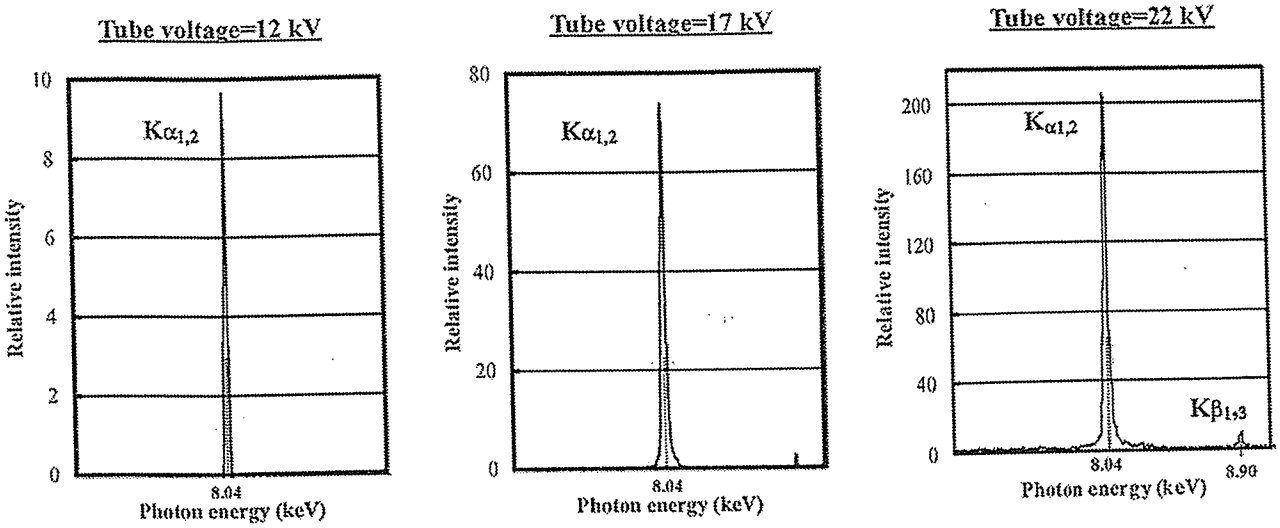

Fig. 5. Measured x-ray spectra while changing the tube voltage.

3.2. *X-ray spectra*

Monochromatic x-ray spectra from the copper-target tube were measured by a transmission-type spectrometer with a lithium fluoride curved crystal 0.5 mm in thickness. The spectra were taken by the CR system with a wide dynamic range, and relative x-ray intensity was calculated from Dicom digital data. Fig. 5 shows measured spectra from the copper target. When the tube voltage was increased, the characteristic x-ray intensity of Kα lines increased.

4. Radiography

The monochromatic radiography was performed with a tube voltage of 17 kV using the filter. Figure 6 shows radiography for imaging a polycapillary plate, and radiograms of the polycapillary are shown in Fig. 7. The center of the black spot in the polycapillary radiogram was mainly imaged by direct transmission beams through capillary holes. As shown in this figure, the spot dimensions increased slightly according to decreases in the PMMA spacer height.

Radiography for imaging a test chart for determining image resolution, and the radio-

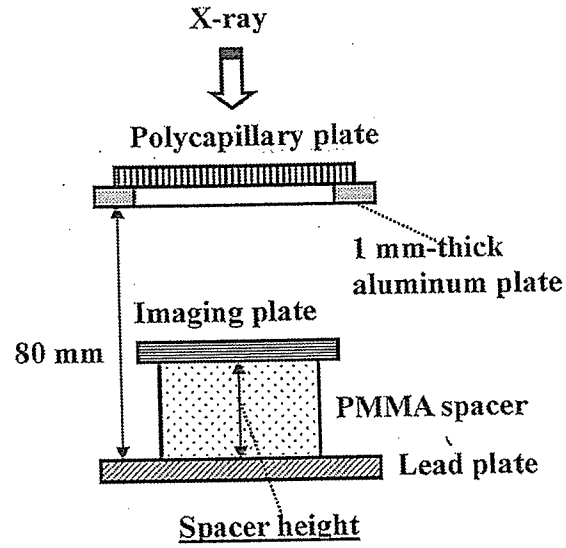

Fig. 6. Radiography for imaging a polycapillary plate while changing the distance between the polycapillary and imaging plates using PMMA spacers.

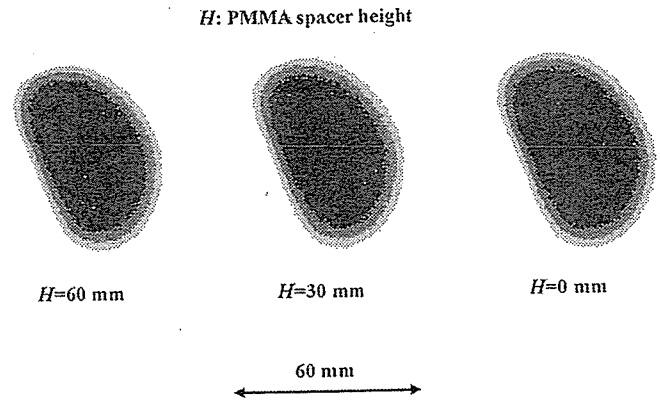

Fig. 7. Radiograms of a polycapillary plate while changing the PMMA height.

grams of 166 μm width lead lines, are shown in Figs. 8 and 9, respectively. Both the image resolution and the line contrast fell with decreases in the spacer height. Figure 10 shows the polycapillary radiography for imaging the test chart; the polycapillary was set on the aluminum plate. With this radiography system, we obtained higher contrast lines as compared with those in Fig. 9. When the spacer height was increased, the image resolution hardly varied, and the image dimensions decreased slightly (Fig. 11).

Figures 12 and 13 show radiography and the radiogram of tungsten wires on a PMMA box, respectively. Although the image contrast increased with increases in the wire diameter, a 50 μm-diameter wire could be observed. The angiography for a rabbit heart is shown in Fig 14; iodine-based microspheres of 15 μm diameter were used, and fine blood vessels of about 100 μm were visible (Fig. 15).

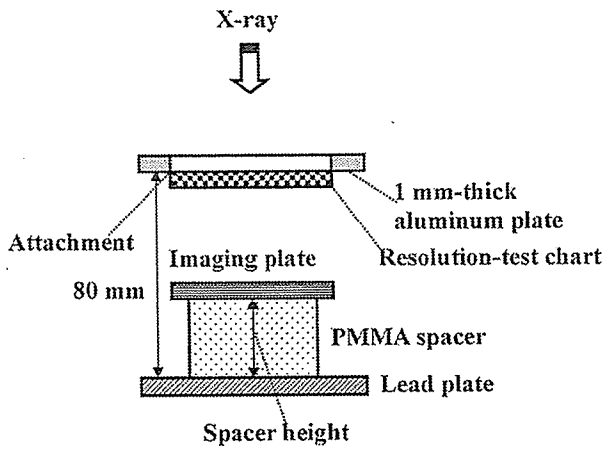

Fig. 8. Radiography for imaging a test chart according to the PMMA spacer height.

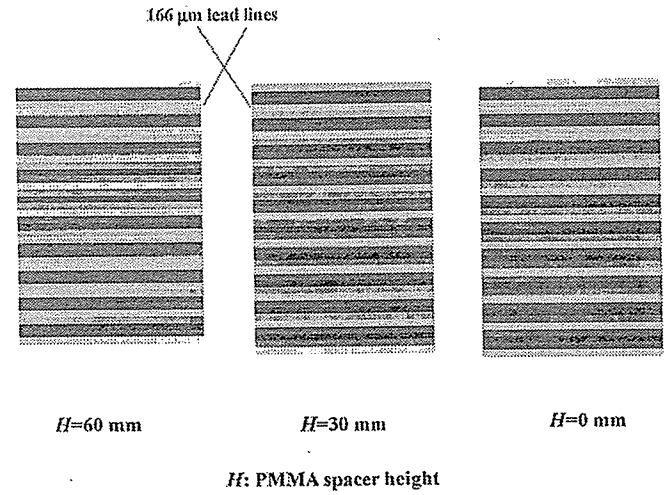

Fig. 9. Radiograms of a test chart according to the PMMA height.

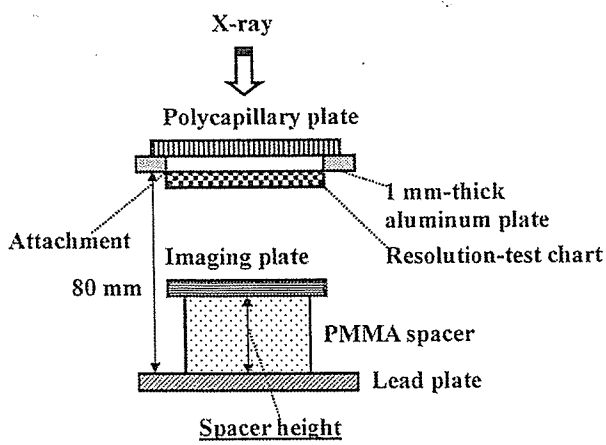

Fig. 10. Radiography for imaging a test chart using a polycapillary plate according to the PMMA height.

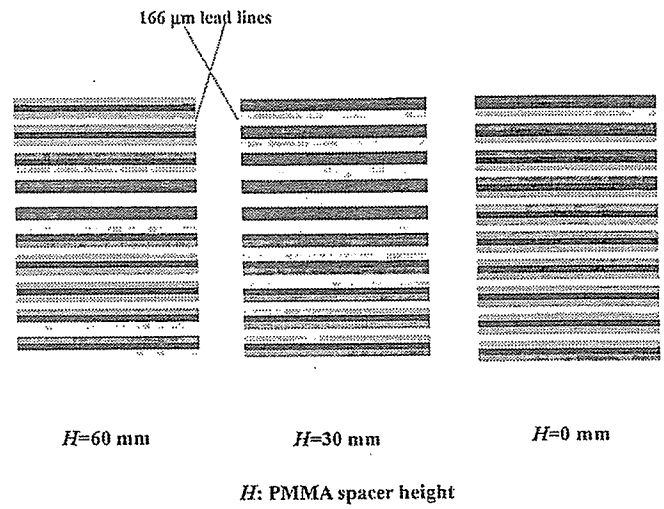

Fig. 11. Radiograms of a test chart using the polycapillary plate according to the PMMA height

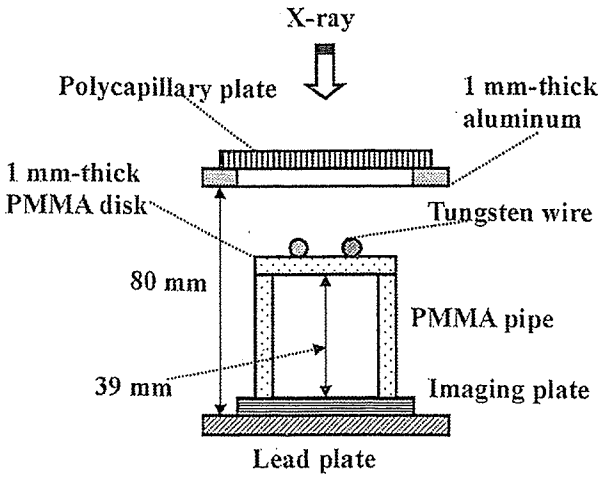

Fig. 12. Radiography for imaging tungsten wires using the polycapillary.

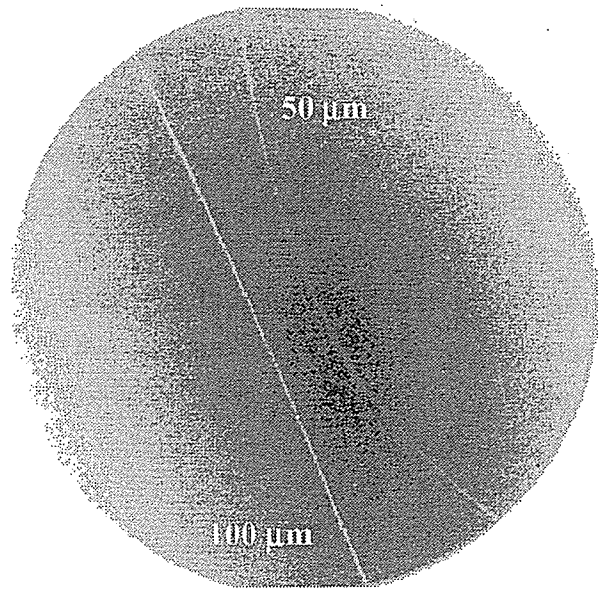

Fig. 13. Radiograms of tungsten wires on a PMMA spacer.

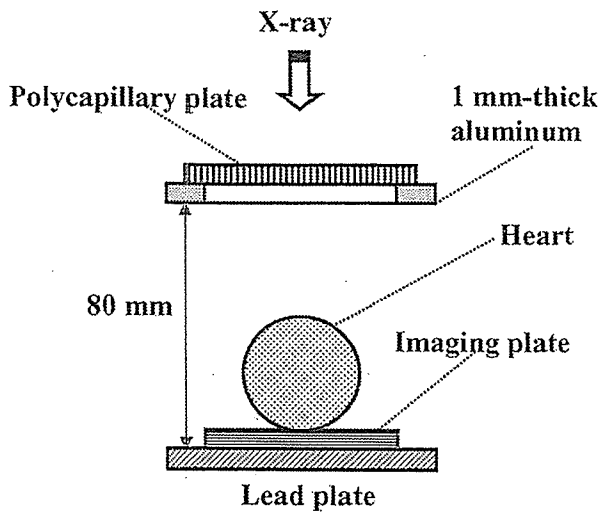

Fig. 14. Angiography using iodine-based microspheres of the heart extracted from a rabbit.

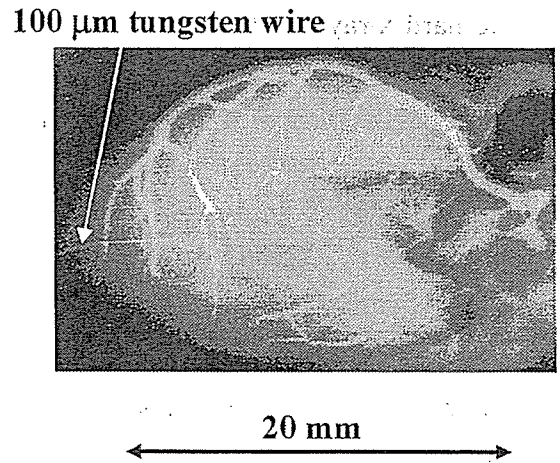

Fig. 15. Angiogram of the heart using the polycapillary.

5. Discussion

In this research, we carried out parallel radiography using a polycapillary plate in conjunction with monochromatic x-rays, and we obtained higher image resolutions as compared with those obtained without using the plate. Currently, the image resolution of the polycapillary is primarily determined by the inner capilliary diameter and the thickness, and it is improved with decreases in the diameter and increases in the thickness. In cases where the CR system is employed, although the resolution of the CR system is primarily determined by the minimum sampling pitch of 87.5 μm, we could observe 50 μm tungsten wires.

The photon energies of the characteristic x-rays are determined by the target element, and the capillary thickness should be increased according to increases in the photon energy because the transmission intensity through capillary glass increases. Subsequently, in order to increase the